Geometry of Cone-beam Reconstruction

by

Xiaochun Yang

B.S., Peking University, 1992

Submitted to the Department of Mathematics
in partial fulfillment of the requirements for the degree of

Doctor of Philosophy

at the

MASSACHUSETTS INSTITUTE OF TECHNOLOGY

February 2002

Author .....
Department of Mathematics
September 26, 2001

Certified by .....
Berthold K.P. Horn
Professor of Electrical Engineering and Computer Science
Thesis Supervisor

Accepted by .....
Daniel J. Kleitman
Chairman, Applied Mathematics Committee

Accepted by .....
Tomasz S. Mrowka
Chairman, Department Committee on Graduate Students

Geometry of Cone-beam Reconstruction

by

Xiaochun Yang

Submitted to the Department of Mathematics
on September 26, 2001, in partial fulfillment of the
requirements for the degree of
Doctor of Philosophy

Abstract

Geometry is the *synthetic* tool we use to unify all existing analytical cone-beam reconstruction methods. These reconstructions are based on formulae derived by Tuy [Tuy, 1983], Smith [Smith, 1985] and Grangeat [Grangeat, 1991] which explicitly link the cone-beam data to some intermediate functions in the Radon transform domain. However, the essential step towards final reconstruction, that is, differential-backprojection, has not yet achieved desired efficiency.

A new inversion formula is obtained directly from the 3D Radon inverse [Radon, 1917, Helgason, 1999]. It incorporates the cone-beam scanning geometry and allows the theoretical work mentioned above to be reduced to *exact* and *frugal* implementations. Extensions can be easily carried out to 2D fan-beam reconstruction as well as other scanning modalities such as parallel scans by allowing more abstract geometric description on the embedding subspace of the Radon manifold. The new approach provides a *canonical* inverse procedure for computerized tomography in general, with applications ranging from diagnostic medical imaging to industrial testing, such as X-ray CT, Emission CT, Ultrasound CT, etc. It also suggests a principled frame for approaching other 3D reconstruction problems related to the Radon transform.

The idea is simple: as was spelled out by Helgason on the opening page of his book, The Radon Transform [Helgason, 1999] — a remarkable duality characterizes the Radon transform and its inverse. Our study shows that the *dual* space, the so-called Radon space, can be geometrically *decomposed* according to the specified scanning modality. In cone-beam X-ray reconstruction, for example, each cone-beam projection is seen as a 2D projective subspace embedded in the Radon manifold.

Besides the duality in the space relation, the symbiosis played between algebra and geometry, integration and differentiation is another striking feature in the tomographic reconstruction. Simply put,

- *Geometry and algebra*: the two play fundamentally different roles during the inverse. Algebraic transforms carry cone-beam data into the Radon domain, whereas, the geometric decomposition of the dual space determines how the differential-backprojection operator should be systematically performed. The reason that different algorithms in

cone-beam X-ray reconstruction share structural similarity is that the dual space decomposition is intrinsic to the specified scanning geometry. The differences in the algorithms lie in the appearance of algebra on the projection submanifold. The algebraic transforms initiate diverse reconstruction methods varying in terms of computational cost and stability. Equipped with this viewpoint, we are able to simplify mathematical analysis and develop algorithms that are easy to implement.

- *Integration and differentiation*: forward projection is the integral along straight lines (or planes) in the Euclidean space. During the reconstruction, differentiation is performed over the parallel planes in the projective Radon space, a manifold with clear differential structure. It is important to learn about this differential structure to ensure that correct differentiation can be carried out with respect to the parameters governing the scanning process during the reconstruction.

Originating from simple geometric reasoning, we provide new interpretations on the *Tuy-Smith data sufficiency condition* and Finch's *stability constraint* on the source orbit. The true nature of the locality in 3D reconstruction is discussed.

Rigorous study on the geometric arrangement of the X-ray source during cone-beam scanning and the related sampling mechanism is carried out. It is aimed at enhancing the quality of cone-beam imaging and reducing the patient's radiation exposure by developing more efficient data acquisition techniques.

Thesis Supervisor: Berthold K.P. Horn
Title: Professor of Electrical Engineering and Computer Science

Acknowledgments

My most gracious thanks go to professor Berthold K.P. Horn, my thesis advisor, for lending me an eye for "poetry in mathematics" and a sense of beauty in plain things through his intuitive mind. He staged up two wonderlands for me, in cone-beam CT and optical tomography, while he set rules and goals for the play. These adventures have satisfied both of my curiosity as well as a need to serve the society.

I can never sufficiently thank professor Gilbert Strang — his warmth and support carried me from stage to stage during my Ph.D. journey. This dissertation would not have been completed in its due time without his engaging and constant encouragement. His mathematical teaching and writings speak out in themselves the highest quality of mastery, understanding and wisdom.

I'd like to pay my sincere gratitude and respect to our young and bright instructor Abi Sarkar. I have gained knowledge in statistics through his eloquent and intuitive teaching as well as numerous discussions. His austere excellency in mathematics and a vigorous passion in teaching serve as inspirations for our generation.

I render my special thanks to professor Sigurdur Helgason for generously giving me his time and sharing his insight in the subject of his expertise, to Alan Edelman and Maurice Van Putten for serving in my thesis committee and giving me sound suggestions. My warmest thanks also go to many people I met at tomography conferences or personal visits, particularly, professor Frank Natterer, David Finch, Alan Greenleaf and Alberto Grünbaum from whom I have learned a great deal about tomography. Their good advice helped me to gain the right perspectives with my new studies.

I am deeply indebted to professor Brittan Chance, the most beloved and esteemed in the optical society. His genuine support and attention towards a graduate student sparks enthusiasm and installs faith. The dreams, hopes he helped raise and sustained continue to draw talented people across many disciplines into the daring pursuit of a new tomography, which is more functional, more humane.

My gratitude extends to MIT School of Art and Humanity, for their excellent curriculum,

teaching and nourishing a diverse humanistic life in MIT. I am especially profited from professor Martin Marks' opera and film classes. These learning experiences not only greatly enriched my enjoyment in music and theatrical art, but also gave me a broad sense of humanity.

The everyday interactions and exchanges with students in Mathematics Department, Artificial Intelligence Laboratory and the larger MIT community have helped my academic and intellectual development. I would like to express my gratitude to Bojko Bakalov, Sergei Bashinsky, Ana-Maria Castravet, Anda Degeratu, Paul Fiore, Benjamin Joseph, Zuoliang Hou, Thomas Minka, Lauren O'Donnell, Dana Pascovici, Alex Perlin and Lizhao Zhang. I am particularly grateful to Wei Luo, Huizhen Yu and Lilla Zollei for reading my thesis and giving helpful input.

I would also like to thank my wonderful and beautiful international friends — Annette Klein, Stanislaw Jarecki, Benjamin Joseph, Juan Lin, Alice Liu, Annika Malmsten, Becky Masterson, Anna Panova, Dana Pascovici, Alex Perlin, Nathan Willcox, Louis Zechtzer ... for many interesting conversations, companions, fun trips, concerts and theaters. You have planted in me an intimacy with the world culture. Our shared love in art and literature is essential to my growth.

For many personal reasons I'd like to thank the following people:

- Chak, Nancy and your big, happy musical family. The decent warmth and cares you had showered me made my short stay in California a long lasting memory.
- My music teacher Holly, for your immense generosity in sharing your art and enormous kindness. The hours I have spent in your studio were some of the happiest during my Ph.D. years.
- My decade(s) old friends Xueqiong, Wei, Honghui, Jianmei, Yi, Ce and Hongwei who have made my life continuingly flow with joy.
- My parents, for the unmeasurable strength, depth and breadth carried in your love and support. My love and gratitude in return are unbounded and beyond any word.

Contents

$\mathbb{R}$	real numbers
$\mathbb{R}^+$	positive real numbers
$\mathbb{R}^n$	n-dimensional Euclidean space
$\mathbf{P}^n$	n-dimensional projective space
$\tilde{\mathbb{R}}^n$	the map of $\mathbf{P}^n$ via $(l, \beta) \to l\beta$
$\mathbf{S}^{n-1}$	$(n-1)$-dimensional unit sphere in $\mathbb{R}^n$
$\mathcal{S}$	Schwartz space
C^∞	space of infinitely differentiable functions
l	the radial distance of a hyperplane in $\mathbb{R}^n$ from the origin
$\boldsymbol{\beta}$	the unit normal of a hyperplane in $\mathbb{R}^n$
$\boldsymbol{\beta}^\perp$	subspace orthogonal to $\boldsymbol{\beta}$
$\boldsymbol{L}_{l,\boldsymbol{\beta}}$	a hyperplane in $\mathbb{R}^n$ with unit normal $\boldsymbol{\beta}$ and radial distance l
Rf	Radon transform of f
$\mathcal{H}$	Hilbert transform
$h_\epsilon(l)$	ramp filter
$F_{\boldsymbol{x}\to\boldsymbol{\xi}}$ or $F_{\boldsymbol{x}}$	nD Fourier transform w.r.t. $\boldsymbol{x}$
$F_{l\to\rho}$	one-variable Fourier transform w.r.t. l
∇	the gradient operator
$\boldsymbol{X}f$	X-ray transform
$\boldsymbol{D}f$	divergent ray transform
$\boldsymbol{P}f$	ray transform function with homogeneous degree 0
$\Omega = supp(f)$	support of f
$\lambda \in \Lambda$	source orbit parameter
$\boldsymbol{\Phi}(\lambda)$	parameterized source orbit
O	the origin, also the object center
O'	the projection of the origin to the center of the image plane
P_1P_2	intersection line between a Radon plane and the image plane
SC	the central ray on a fan-beam slice
r, θ	the polar coordinates on a fan-beam slice
α	angle of the slice
s	the radial distance from an intersection line on the image plane to the image center O'
H_λ	the homogeneous space induced by a single cone-beam projection
$\boldsymbol{P}^2_\lambda$	the 2D projective space of 2D planes passing by a point source
$\boldsymbol{R}(\lambda)$	the orthonormal moving frame matrix
Im	imaginary part
S	the sphere that encloses supp(f)
$\hat{S}$	Fourier spectral sphere
$\boldsymbol{\gamma}$	normalized principal direction, or plane orientation
$\boldsymbol{L}_{\boldsymbol{\gamma}}$	projection plane oriented at $\boldsymbol{\gamma}$
$\hat{\boldsymbol{L}}_{\boldsymbol{\gamma}}$	spectral plane oriented at $\boldsymbol{\gamma}$
$C_{\boldsymbol{\gamma}}$ and $\hat{C}_{\boldsymbol{\gamma}}$	great circles oriented at $\boldsymbol{\gamma}$
$\boldsymbol{\tau}$	great circle on the backprojection sphere
$\boldsymbol{\varsigma}$	characteristic curve
$\tilde{\boldsymbol{\varsigma}}$	projection of $\boldsymbol{\varsigma}$ onto a horizontal plane through the origin

List of Figures

Chapter 1

Introduction

1.1 The Problem and Motivations

The problem in cone-beam computerized tomography (CT) is the recovery of the density function of a 3D object from a set of *cone-beam projections*. Such a system uses an area detector to receive the rays emitted from an X-ray point source and attenuated by partial absorption in the object that they pass through. As in traditional (planar) CT, the source and the detector are placed on opposite sides of the object being scanned. Rays contributing to an image on the detector surface form a cone with the X-ray source at the apex (Fig. 1-1). From the X-ray radiance value recorded at a point on the area detector one can compute the integral of attenuation along the ray from the X-ray source to the given point on the detector.

For convenience of exposition, we replace the detector array with an *image plane* perpendicular to the *principal direction*, a line connecting the X-ray source to the origin (typically the center of the object). By doing so, we avoid the need to address the specific arrangement of individual detector configuration. A coordinate transformation is then required to map a particular detector surface onto the chosen standard image plane.

In order to obtain many different *views* of the object, the source-detector pair may be mounted on a rotational cylindrical gantry and the tested object may also undergo a si-

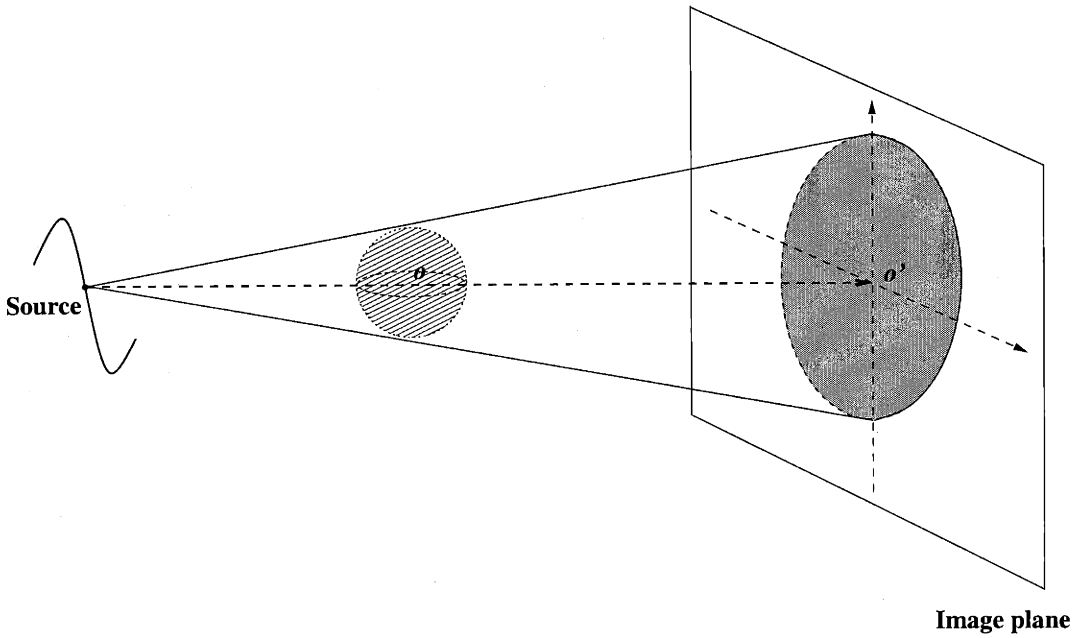

Figure 1-1: *Illustration of a cone-beam projection: the image plane is perpendicular to the principal direction which connects the source to the center of the object.*

multaneous translation — it is as if the X-ray source and the detector travel together on a smooth 3D curve while remaining at a fixed position relative to one another. This curve followed by the X-ray source relative to the object being scanned is called the *source orbit.* A sequence of 2D cone-beam images projected from various source positions can be acquired and used to reconstruct the distribution of absorption inside the 3D object.

Mathematically speaking, cone-beam reconstruction is the recovery of a function, f on $\mathbb{R}^3$, by a collection of its line integrals emitting from a space curve. It can be treated as a specific Radon problem [Radon, 1917, Helgason, 1999] with incomplete data in the sense that only a *subset* instead of *all* of the line integrals are available.

The 3D cone-beam imaging system is currently progressing to take over the conventional multi-slice 2D machines because of its many attractive qualities: faster scans, higher patient's throughput, significant reduction in X-ray dosage, and isotropic resolution. It also has great potential to enhance the speed and accuracy of CT imaging while lowering hazardous radiation exposure.

1.2 Previous Work

Ever since Hounsfield delivered the first CT machine in 1972, CT technology has received broad acceptance as a reliable means to inspect otherwise inaccessible internal structures by both medical and industrial communities. A 1979 Nobel prize was awarded to Hounsfield and Cormack for their landmark contributions to the invention and algorithmic development of the first-generation CT.

Among all the creative involvement leading to cone-beam CT, Radon's 1917 paper is the resilient fountainhead [Radon, 1917]. It solved the problem of recovering a 2D function f from all of its line integrals (known as the X-ray transforms in modern time), denoted by Xf, as well as a version of the 3D problem in which the building blocks of the inverse reconstruction are all of the 2D planar integrals of f, denoted by Rf (which is later called the Radon transform of f). His simple and classical results have grown roots into an interesting branch of mathematics, integral geometry. Those same results, germ to modern diagnostic medicine, continue to nurture a benevolent growth in the medical imaging society.

The original Radon paper provides the most lucid description and derivation of the Radon transform and its inverse. A deep and extensive theoretical development and reference on the Radon transform is given by Helgason [Helgason, 1999].

Under the circumstances of tomographic reconstructions, only a subset of *line integrals* is obtained from X-ray scans. Such tasks, nevertheless, are treated as Radon problems because their main results still rely on the Radon transform theorem. Everyone, who has spent some time with the Radon transform, would discover from it a wellspring of mathematical ideas and an unfailing beauty. The many attractions of the Radon transform are partly due to Radon's simple and explicit inversion formula, partly due to the rich dualities and cascaded hierarchies inherent in the geometric structure. It has been adapted to several 2D scanning geometries such as those in parallel-beam and fan-beam CT.

Natterer's book [Natterer, 1986] provides a comprehensive and eloquent account on mathematical studies in computerized tomography.

Horn's two seminal papers [Horn, 1978, Horn, 1979] represent a prime development in 2D

image reconstruction that occurred when the earlier parallel scans were replaced by the faster and more effective fan-beam data acquisitions. His insight is that an inversion formula could be written regardless of the ray sampling schemes. Whereas, only for certain sampling geometries, proper local scanning coordinates yield a simpler and factorable *Jacobian*. Consequently, reconstruction can be implemented in the favorable fashion of summation-filtered-backprojection. The prominent example is the fan-beam reconstruction.

Now, a renewed initiative is in the direction of replacing multi-slice 2D scans by the even more efficient 3D cone-beam data collections.

From a geometric point of view, 2D fan-beams and 3D cone-beams share common features in the sense that the *divergent* rays emitting from a single source point constitute a projective subspace in the Radon transform domain, and, in both cases, the X-ray source travels on a 1D manifold. However, algorithms developed for 2D and 3D reconstruction so far bear little resemblance in their overall structure.

The principal difficulty encountered in the 3D reconstruction is caused by the sophisticated mapping from the local projection geometry to the Radon space geometry, especially when non-planar source orbit is used. Unfortunately, such an orbit is required for exact reconstruction in 3D. Besides, 3D volumetric data is inherently bulky and difficult to manage. Without a clear understanding of the unique structure intrinsic to the problem, data manipulation and storage may lead to exceedingly high computational cost.

The mainstream approach in the early days of 3D reconstruction was based on approximation. For example, rebinning divergent rays to parallel rays so that the reconstruction algorithm for parallel-beams based on the Fourier-slice theorem can be applied. Such reconstruction methods are characterized by excessive computational and structural complexity. Furthermore, reconstruction error introduced by the rebinning is difficult to track down and therefore hard to remediate. It leads to poor reconstruction performance.

The first practical and well-known filtered backprojection (FBP) cone-beam reconstruction algorithm is given by Feldkamp (FDK) et al. [Feldkamp, 1984] for circular source orbits. In such a case, data from cone-beams with narrow angles is treated in an *approximate* way using *ad hoc* extensions of 2D fan-beam methods. The FDK algorithm is easy to implement,

however, it only gives reasonably good reconstruction near the mid-plane and cannot be used for wide cone angles. As we shall see, the planar source orbit postulated here does not provide enough information of the Radon transform that is needed for exact reconstruction.

The excellent work of Tuy [Tuy, 1983], Smith [Smith, 1985] and Grangeat [Grangeat, 1991] laid out the theoretical foundation for *exact* cone-beam reconstruction by deriving analytical inversion formulae as well as the critical *data sufficiency condition.* Together they pictured a bigger frame of mathematics relevant for solving the cone-beam problem — Radon transform is still behind all these achievements, although in Tuy's formulation, it is almost completely concealed by the Fourier transform. These derivations indeed add new perspectives to our understanding of the Radon transform.

As early as 1961, Kirillov derived an inversion formula for the complex-valued functions under cone-beam geometry [Kirillov, 1961]. It requires an infinite source orbit, which is certainly not met in practice. Following Kirillov's derivation, Tuy gave the first, practically useful, cone-beam inversion formula for real-valued functions in 1983 [Tuy, 1983]. This was also the first time that the *data sufficiency condition* became explicit: *all or almost all planes intersecting the object should meet with the source orbit.* Tuy's formulation has a classical touch of Fourier analysis. We will detail some of the subtle links between the Radon transform and the Fourier transform in section 3.3.2.

Smith and Grangeat's cone-beam inversion formulae are both cast in the framework of the Radon transform theorem. They have established connections between the cone-beam data and the $2nd$-order radial derivative of the Radon transform, $R''f$, through some intermediate functions in the Radon transform domain. As a result, Radon's inversion formula can be evoked. Note that the $2nd$-order radial derivative of the Radon transform is needed in order to use the 3D Radon inversion formula — $R''f$ is then backprojected to recover f.

Smith's intermediate function is the Hilbert transform, $\mathcal{H}_l\{R'f\}$, of the $1st$-order radial derivative of the Radon transform. It can be *filtered* over the parallel planes to obtain $R''f$. In the case of Grangeat's formulation, the $1st$-order radial derivative, $R'f$, serves as an implicit link between the cone-beam data and $R''f$.

A breakthrough insight in these early derivations is that the data collected while the X-ray

source moves on a 3D curve (a 1D manifold) is sufficient for exact reconstruction. That is, it is *not* necessary for the source to be placed at every point on a specific 3D surface (a 2D manifold) encompassing the 3D object.

Another important point is that inversion is possible even though the Radon transform itself is not available. This is good since a nontrivial integral equation [Gelfand, 1986] need to be solved in order to obtain planar integrals from cone-beam projections.

Although the cone-beam problem is mathematically solved, there is so far *no exact implementation* available. It is not clear how the differential (or filtered)-backprojection operator can be discretized for Tuy, Smith and Grangeat's analytical inversion formulae.

Motivated by the earlier theoretical results, attempts have been made in the last decade by many groups to derive true 3D cone-beam reconstruction algorithms. Most of them are based on Grangeat's *Fundamental Relation*, in which, the weighted line integral of each slice of fan-beams inside the recessive cone is related to the first radial derivative of the Radon transform, $R'f$. The second radial derivative of the Radon transform is thereby determined. Examples include the cone-beam algorithm proposed by Grangeat himself using Marr's approach [Marr, 1981] to invert the Radon data [Grangeat, 1991]. Axelsson and Danielsson [Axelsson, 1994] further improved Grangeat's algorithm by using the Fourier linogram method to speed up the transfer of cone-beam data into the Radon transform domain.

The major disadvantage of the above Radon-based algorithms is that intermediate resampling and interpolation in the Radon space are needed. Furthermore, reconstruction can only start after all of the cone-beam data is collected.

More recent works on obtaining relatively efficient FBP-typed algorithms [Kudo, 1994, Defrise, 1994, Wang, 1999] have shown some promises. However, a common misconception, primarily due to an unfamiliarity with the topological and differential structure of the Radon space (a non-Euclidean manifold), hampers their success.

The analytical inversion formulae mentioned above are based on continuous data, while in practice, the orbit is sampled (we only take images with the source positioned at a finite number of points along the orbit), and each image in turn is also sampled (using a discrete

grid of detectors). This discretization leads to degradations and artifacts that have not been well understood mathematically because discrete sampling can not be introduced into Tuy, Smith and Grangeat's intermediate-staged inverse formulations. There is as yet no precise mathematical model to address this problem.

Sampling geometry for nonplanar source orbit has not been explored. As a result, the subject of effective data-acquisition techniques for cone-beam imaging has not matured. In many cases, the image quality available from existing cone beam reconstructions remains inferior to that of single slice fan beam reconstructions.

As with most *inverse problems*, the cone-beam reconstruction may only be possible if the data collection satisfies additional conditions. It may also be subject to *ill-posedness*, i.e., large amplification of inevitable measurement noise in the data by the reconstruction method. A remaining and very important issue then is the characterization of the source orbit that minimizes the noise amplification in reconstruction and that samples the transform space most efficiently.

Overall, optimization in reconstruction efficiency and stability among the exact cone-beam methods need to be further studied and understood.

1.3 A Few Goals of the Thesis

This thesis is aimed at developing efficient and easy to implement cone-beam reconstruction algorithms based on an analytical approach. A second goal is to develop a good data-acquisition strategy in order to help reduce the needed X-ray exposure for a given image quality.

Our research is a continuation of Tuy, Smith and Grangeat's theoretical work on cone-beam reconstruction. Their intermediate functions, obtained *within* a projection, should be viewed as the first stage of the inverse procedure. Our focus instead is on the second stage, *across* the projections, that essentially brings us to the final reconstruction.

The results we obtained is also an extension, in dimension, from Horn's general inverse formulation for arbitrary sampling schemes in 2D to a principled approach for a true 3D

cone-beam reconstruction. Such a frame is general enough to accommodate various scanning geometries in both 2D and 3D. Furthermore, our understanding of the nature of 3D reconstruction shows that there is a geometric inheritance in tomographic reconstruction passed from lower to higher dimensions. In this thesis, the *geometric principle* that governs the process of tomographic reconstruction will be developed.

Aside from the practical and mathematical aspects of our considerations above on the cone-beam problem within the framework of Radon transform theorem, some extraordinary findings lie in its unique *mathematical aesthetics.* Some observations are:

(1) Geometry and algebra each has its own interesting life thread in this particular problem. Their fruitful union is embodied in the simple and nice differential property of the Radon transform. We want to show their true relations in the context of cone-beam geometry.

(2) Geometric touch is incredibly vivid: several different kinds of geometries alternatively come into the scene. When their fundamental structures and interaction are understood, simple algorithms can be easily derived.

(3) Moreover, it is revealed that the Radon transform theorem has one of the richest compositions of duality, in both geometry and algebra. This particular aspect will be explored in our full capacity.

1.4 Thesis Organization

Here is how this thesis is organized:

- Chapter 2: This chapter provides the required mathematical background — the Radon transform theorem and how it can be applied to 2D and 3D tomographic reconstructions. The general geometric context for cone-beam reconstruction is presented.

- Chapter 3: The focus of this chapter is a thorough analysis of three cone-beam inversion formulae derived by Tuy, Smith and Grangeat. Section 3.1 presents the main

results obtained by Tuy and Smith. A new, simplified proof of Grangeat's *Fundamental Relation* is given in section 3.2. We then undertake, in section 3.3, a mathematical equivalence study using Fourier analysis. It has been shown that Tuy, Smith and Grangeat's intermediate functions are all related to the first differential form of the Radon transform *within* a cone-beam projection. Results are obtained in the more general n-dimensional space. The purpose is to demonstrate the applicability of similar reconstructions to various scanning geometries in 2D, 3D, or even nD, when the source apex moves on a 1D manifold. Some subtle relationships between the Radon transform and the Fourier transform are also revealed.

- Chapter 4: Section 4.1 studies the internal geometric structure of the cone-beam problem. The key ideas are *decomposition* and *embedding*. Each 2D divergent-ray projection is a projective, embedding subspace in the Radon manifold. Section 4.2 presents the key result of this thesis — *the canonical cone-beam inversion formula*. It achieves the Radon space decomposition in an analytical form. After mapping out the differential structure of the Radon manifold with respect to the parameter governing the scanning process in section 4.3, we provide in section 4.4 a unified inverse procedure which would carry Tuy, Smith and Grangeat's intermediate functions toward the final reconstruction. It results in a family of *exact*, *FBP-typed* cone-beam reconstruction algorithms. This chapter bridges the previous theoretical work with practical implementation. The resulting algorithms are very easy to understand and implement with complexity level in the order of $O(mn^3)$ (where n is the edge size of the volumetric data and m depends on the number of projections). Section 4.5 is a general discussion on tomographic reconstructions. By allowing more abstract geometric description of the embedding subspace on the Radon manifold, the inverse procedure presented earlier can be adjusted and used in a variety of scanning geometries.

- Chapter 5: This chapter provides a few critical mathematical devices for studying the Radon space sampling mechanism related to the geometrical properties of the source orbit. The main concept lies in the *method of moving frames*: each great circle on the backprojection sphere (a Radon sphere) undergoes rigid 3D motions relative to the X-ray source moving on the orbit. We demonstrate it through the sinusoidal orbit.

Chapter 2

Mathematical Background

Cone-beam reconstruction has an elegant mathematical foundation — the *Radon transform theorem.* As we walk through Tuy, Smith and Grangeat's inverse formulations, it becomes clear that the Radon transform has gradually stepped out of the shadow of the Fourier transform. It gives rise to an increased geometric transparency.

Our analysis of Tuy, Smith and Grangeat's formulae relies on the Radon transform and its inverse. This chapter provides the required mathematical background, as well as the geometric context we used to approach the cone-beam reconstruction problem.

2.1 The Radon Transform and Its Inverse

The Radon transform of a function f on $\mathbb{R}^n$ is the set of integrals of f over the hyperplanes of dimension $n-1$ in $\mathbb{R}^n$. In the 2D case, as in the traditional slice-at-a-time CT, the integrals in the Radon transform are along lines. In the 3D case, appropriate for cone-beam CT, the integrals are over planes.

A **hyperplane** in $\mathbb{R}^n$ is determined by its unit normal vector $\boldsymbol{\beta}$ and its perpendicular distance l from the origin,

$$\boldsymbol{L}_{l,\boldsymbol{\beta}} := \left\{ \boldsymbol{x} \in \mathbb{R}^n \mid \boldsymbol{x} \cdot \boldsymbol{\beta} = l,\ l \geq 0,\ \boldsymbol{\beta} \in \mathbf{S}^{n-1} \right\}, \tag{2.1}$$

where "$\cdot$" denotes the inner product and $\mathbf{S}^{n-1}$ denotes the $(n-1)$D unit sphere in $\mathbb{R}^n$.

The **Radon transform** of f can therefore be conveniently expressed as a function of two parameters (l and $\boldsymbol{\beta}$):

$$Rf(l,\boldsymbol{\beta}) := \int_{\boldsymbol{x}\in\left\{\boldsymbol{x}|\boldsymbol{x}\cdot\boldsymbol{\beta}=l\right\}} f(\boldsymbol{x})\,d\boldsymbol{x}, \tag{2.2}$$

where the integration plane is $\boldsymbol{L}_{l,\boldsymbol{\beta}}$.

The **Radon space** then is the space $\mathbf{P}^n = \mathbb{R}^+ \times \mathbf{S}^{n-1}$ of all hyperplanes in $\mathbb{R}^n$. However, sometimes, the symmetric space $\mathbb{R} \times \mathbf{S}^{n-1}$ provides extra analytical convenience and therefore is desirable. A potential problem is that the mapping $(l,\boldsymbol{\beta}) \to \boldsymbol{L}_{l,\boldsymbol{\beta}}$ from $\mathbb{R} \times \mathbf{S}^{n-1}$ to $\mathbf{P}^n$ is not bijective, since $(l,\boldsymbol{\beta})$ and $(-l,-\boldsymbol{\beta})$ identify the same hyperplane. This can be easily resolved by extending the Radon transform Rf as an even function, that is, $Rf(-l,-\boldsymbol{\beta}) = Rf(l,\boldsymbol{\beta})$.

Under certain smoothness conditions, i.e., $f \in \mathcal{S}(\mathbb{R}^n)$, in the Schwartz space, Rf is differentiable on $\mathbf{P}^n$. The derivative of Rf with respect to its first parameter, l, is customarily called the **radial derivative**.

The **Schwartz space** $\mathcal{S}$ is defined as the functional space on $\mathbb{R}^n$ such that for $f \in \mathcal{S}(\mathbb{R}^n)$,

(1) $f \in C^\infty(\mathbb{R}^n)$, the space of continuous, infinitely differentiable functions;

(2) f and all its derivatives are rapidly decreasing:

$$\sup|\boldsymbol{x}|^{\boldsymbol{i}}|\partial_{\boldsymbol{x}}^{\boldsymbol{j}} f(x)| < \infty \tag{2.3}$$

for any multi-indices $\boldsymbol{i} = (i_1, i_2, \cdots, i_n)$ and $\boldsymbol{j} = (j_1, j_2, \cdots, j_n)$, where i_k's and j_k's ($k = 1, 2, \cdots, n$) are all non-negative integers. The mixture derivative $\partial_{\boldsymbol{x}}^{\boldsymbol{j}}$ denotes $\dfrac{\partial^{j_1+j_2+\cdots+j_n}}{\partial_{x_1}^{j_1}\partial_{x_2}^{j_2}\cdots\partial_{x_n}^{j_n}}$ where $\boldsymbol{x} = (x_1, x_2, \cdots, x_n)$.

We will assume $f \in \mathcal{S}(\mathbb{R}^n)$ throughout our discussion, but we should also be aware of the fact that this assumption can be relaxed, i.e. to Sobolev space, in many situations.

For the purpose of easy visualization, one can map $\mathbf{P}^n$ onto $\mathbb{R}^n$ using $(l,\boldsymbol{\beta}) \to l\boldsymbol{\beta}$. Note that this mapping is singular at the origin, since it is not possible to recover the direction

of β from $l\beta$ when $l = 0$. Let $\tilde{\mathbb{R}}^n$ denote the target space, in distinction with the familiar Euclidean space. Then each hyperplane in $\mathbb{R}^n$ corresponds to a **Radon point** in $\tilde{\mathbb{R}}^n$. In this target space, one can imagine a set of concentric spheres centered at the origin. For a given point $P \in \tilde{\mathbb{R}}^n \backslash \{0\}$, the spherical local chart seems to be convenient. It consists of a radial component, l, and a $(n-1)$-dimensional basis on the plane tangent to the sphere containing P (Fig. 2-1). This local chart is called the geodesic chart.

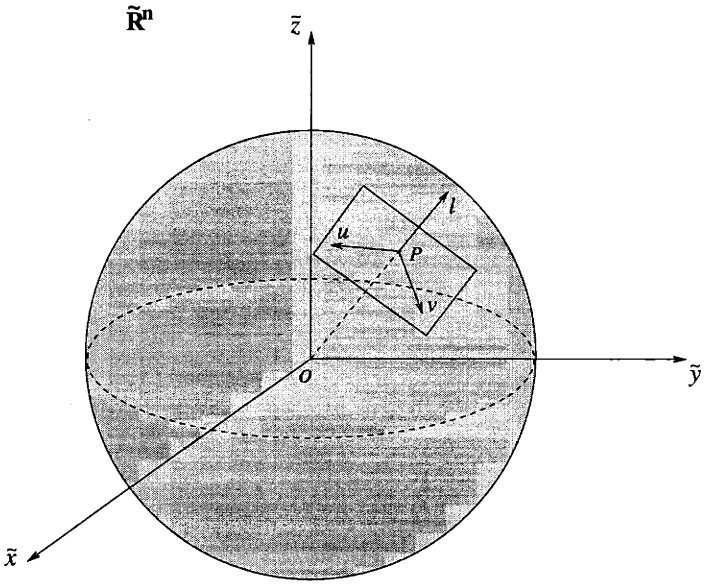

Figure 2-1: *The Radon space* $\mathbf{P}^n$ *is mapped to* $\tilde{\mathbb{R}}^n$ *with a singularity at the origin. The local chart illustrated here is called the geodesic chart.*

On the other hand, contrary to the common practice, we do not recommend using $\tilde{\mathbb{R}}^n$ as a working space in tomographic reconstruction, since $\tilde{\mathbb{R}}^n$ is a *nongeneric* representation of $\mathbf{P}^n$. It is easy to check that the sampling conditions in $\tilde{\mathbb{R}}^n$ do not reflect the sampling conditions in $\mathbf{P}^n$. Furthermore, it gives us a *distorted perception* of the topological relationships among the space $\mathbf{P}^n$ and subspaces of $\mathbf{P}^n$. For example, the projective subspace $\mathbf{P}^{n-1}$ containing all hyperplanes intersecting at one point, say $\boldsymbol{x}$, manifests itself as a curved surface in $\tilde{\mathbb{R}}^n$. Under the action of linear group transformations, the subspace $\mathbf{P}^{n-1}$ undergoes a rigid motion. In accordance, the curved surface, as seen in $\tilde{\mathbb{R}}^n$, deforms and changes position. It is in fact difficult to describe both $\mathbf{P}^{n-1}$ and its global evolutions in $\tilde{\mathbb{R}}^n$. Some of the failures in previous attempts at deriving cone-beam reconstruction algorithms can be attributed to this inappropriate representation.

Alternatively, one can visualize the Radon space $\mathbf{P}^n$ in the object space, i.e., by attaching to each point, $\boldsymbol{x} \in \mathbb{R}^n$, a $(n-1)$D unit sphere. Denote this sphere by $\mathbf{S}_{\boldsymbol{x}}^{n-1}$, where $\boldsymbol{x}$ is considered as an index. This visualization uses points on $\mathbf{S}_{\boldsymbol{x}}^{n-1}$ to represent the unit normals of all the hyperplanes through $\boldsymbol{x}$. We call such a sphere a **Radon sphere**, or **backprojection sphere** when the inverse of the Radon transform is discussed.

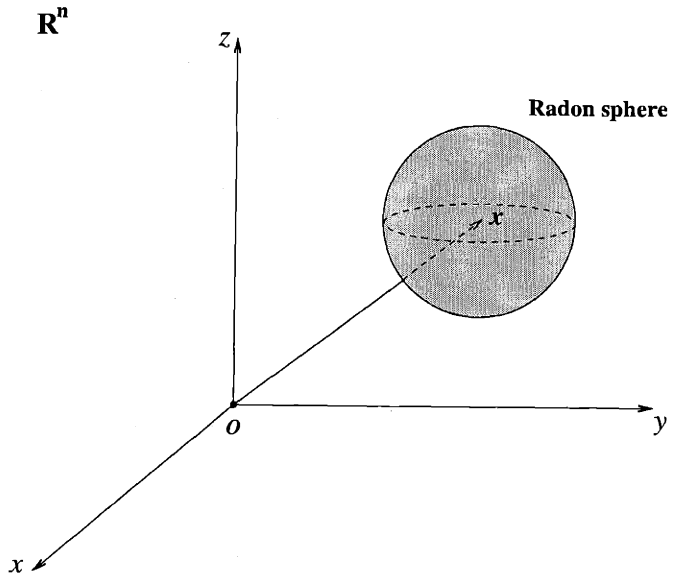

Figure 2-2: *Visualization of the Radon space in the object space.*

Recovering a function $f \in \mathcal{S}(\mathbb{R}^n)$ from its Radon transforms is called the **inverse Radon transform**. The following inversion formula is given in [Helgason, 1999, Natterer, 1986]:

Theorem 2.1 *The function $f \in \mathcal{S}(\mathbb{R}^n)$ can be recovered from its Radon transform Rf by*

$$f(\boldsymbol{x}) = \begin{cases} \frac{1}{2}(2\pi)^{1-n}(-1)^{(n-2)/2} \int_{\mathbf{S}^{n-1}} \frac{\partial^{n-1}}{\partial l^{n-1}} Rf(l,\boldsymbol{\beta})\Big|_{l=\boldsymbol{x}\cdot\boldsymbol{\beta}} d\boldsymbol{\beta}, & \text{for odd } n \\ \frac{1}{2}(2\pi)^{1-n}(-1)^{(n-1)/2} \int_{\mathbf{S}^{n-1}} \mathcal{H}_l\Big(\frac{\partial^{n-1}}{\partial l^{n-1}} Rf(l,\boldsymbol{\beta})\Big)\Big|_{l=\boldsymbol{x}\cdot\boldsymbol{\beta}} d\boldsymbol{\beta}, & \text{for even } n \end{cases} \tag{2.4}$$

where $\mathbf{S}^{n-1}$ is the $(n-1)D$ unit sphere and $\mathcal{H}$ is the Hilbert transform, defined by

$$\mathcal{H}(h)(s) = \frac{1}{\pi} \int_{-\infty}^{\infty} \frac{h(l)}{s-l}\, dl. \tag{2.5}$$

The above integral is considered as the Cauchy principal value. One can think of the Hilbert transform as a convolution with $1/(\pi s)$.

Note that the integral in Eqn. (2.4) over $\mathbf{S}^{n-1}$ is the **backprojection** operator — it integrates over all the hyperplanes passing by $\boldsymbol{x}$. The integration sphere is therefore called the **backprojection sphere** with its center at $\boldsymbol{x}$. The backprojection sphere agrees with the Radon sphere we defined earlier.

Also note that the Radon transform integrates over all points on a hyperplane, while the backprojection integrates over all hyperplanes through a point. It is in this sense that backprojection is known as the **dual operator** of the Radon transform, and the Radon space is called the **dual space** of the Euclidean space $\mathbb{R}^n$.

The original inversion formulae for the 2D and 3D cases were given by Radon in his 1917 paper [Radon, 1917]. In the same paper, generalization was considered in several directions. One is the inverse of similar integal transform in higher dimensional space, and the other is towards the inverse reconstruction of integrals over curves or surfaces.

Interestingly, inverting the Radon transform differs fundamentally in odd and even dimensional space: in odd dimensions, it acts more locally in the sense that the result at a particular point depends only on the Radon transforms on the hyperplanes near that point. Whereas, in even dimensions, the inversion is not local since the Hilbert transform is a global operation.

2.2 Properties of the Radon Transform

Important properties of the Radon transform include [Helgason, 1999, Poularikas, 2000]:

- *Differential property:*

$$R\Big\{\boldsymbol{a}\cdot\nabla f\Big\}(l,\boldsymbol{\beta}) = \boldsymbol{a}\cdot\boldsymbol{\beta}\frac{\partial Rf(l,\boldsymbol{\beta})}{\partial l}, \tag{2.6}$$

where $\boldsymbol{\alpha}$ is an arbitrary vector in $\mathbb{R}^n$ and ∇ denotes the gradient.

- *Central Slice Theorem:*

$$F_{\boldsymbol{x}\to\boldsymbol{\xi}}\{f\}(\rho\boldsymbol{\beta}) = F_{l\to\rho}\{Rf\}(\rho,\boldsymbol{\beta}), \tag{2.7}$$

where $F_{\boldsymbol{x}\to\boldsymbol{\xi}}$ denotes the nD Fourier transform, and $F_{l\to\rho}$ denotes the 1D Fourier transform with respect to the radial parameter.

The *differential property* relates the Radon transform of the directional derivative to the derivative of the Radon transform. Note that the coefficient $\boldsymbol{\alpha}\cdot\boldsymbol{\beta}$ is the projection of $\boldsymbol{\alpha}$ onto the unit normal vector $\boldsymbol{\beta}$ of the hyperplane. This property implies a powerful link between the algebraic integral transform of the scalar derivative field, $\boldsymbol{\alpha}\cdot\nabla f$, and the geometric relations in connection with the Radon transform Rf. We will see it applied to our proof of the *Fundamental Relation* (see section 3.2) which lies at the heart of cone-beam reconstruction.

The *Central Slice Theorem* establishes the link between the Radon transform and the Fourier transform — the nD Fourier transform of a function f is the 1D Fourier transform of its Radon transform. This property has been widely used in the parallel-beam tomographic reconstruction.

The close relation between the Radon transform and the Fourier transform is emphasized in [Helgason, 1999]. In fact, the intimate tie between these two transforms provides one of the easiest derivation of the Radon inversion formula (Eqn. (2.4)).

2.3 2D and 3D Reconstructions

For $n = 2$, Eqn. (2.4) is reduced to (see also [Radon, 1917]):

$$f(\boldsymbol{x}) = \frac{1}{4\pi}\int_{\mathbf{S}^1} \mathcal{H}_l\Big(\frac{\partial}{\partial l}Rf(l,\boldsymbol{\beta})\Big)\Big|_{l=\boldsymbol{x}\cdot\boldsymbol{\beta}} d\boldsymbol{\beta}. \tag{2.8}$$

It is clear, for each direction $\boldsymbol{\beta}\in\mathbf{S}^1$, a one-dimensional global convolution needs to be performed. Hence, the value $f(\boldsymbol{x})$ at a particular point depends on *all* of the transform values Rf during the inverse. This non-local character inherent in the 2D Radon transform

inverse is attributed to the Hilbert transform in the formula.

In the planar tomographic reconstruction, the Radon transform $Rf(l,\beta)$ is obtained directly from the X-ray projections:

$$Rf(l,\beta) = \int_{-\infty}^{\infty} f(l\beta + t\beta^{\perp})\, dt, \tag{2.9}$$

where $\beta^{\perp}$ is a unit vector in the direction perpendicular to β.

Using this 2D approach, a 3D volume can be obtained by stacking many 2D slices.

In the case of $n = 3$, Eqn. (2.4) is reduced to (see also [Radon, 1917]):

$$f(\boldsymbol{x}) = -\frac{1}{8\pi^2} \int_{\mathbf{S}^2} \left. \frac{\partial^2 Rf(l,\beta)}{\partial l^2} \right|_{l=\boldsymbol{x}\cdot\beta} d\beta. \tag{2.10}$$

The derivative in the integrand indicates a remarkable locality in the 3D inverse: to compute $f(\boldsymbol{x})$ we need to know only integrals over all planes that are close to $\boldsymbol{x}$. This is distinctively different from the 2D case, where all of the line integrals contribute to the inverse at any reconstruction point.

The quantity we back project here is the second radial derivative $R''f$ of the Radon transform. Hence to use this formula, we need the second radial derivative of the Radon transform, *not* necessarily the Radon transform Rf itself .

Note that the differential-backprojection operator, when evaluated for point $\boldsymbol{x}$, acts on $Rf(l,\beta)$ of all or almost all planes passing through $\boldsymbol{x}$, where $l = \boldsymbol{x}\cdot\beta$, and no other planes.

2.4 The Hilbert Transform

The Hilbert transform appeared in Eqn. (2.8) (for even dimensional case) is a 1D convolution along the radial direction. The resulting transform remains in the Radon domain. Since the convolutional kernel $1/(\pi s)$ is known as a tempered distribution [Helgason, 1999], special care needs to be taken in order to regularize the computation.

The Hilbert transform of a derivative can be best understood in terms of the Fourier trans-

form. Taking the derivative in the radial direction corresponds to multiplying by $i\rho$ in the transform domain, where ρ is the radial frequency. Taking the Hilbert transform corresponds to multiplying by $(1/i)\text{sgn}(\rho)$. Cascading the two operations corresponds to multiplication of their transforms, and it yields

$$i\rho(1/i)\text{sgn}(\rho) = |\rho|. \tag{2.11}$$

This is the transform of the *ramp* filter.

Since the Fourier inverse of $|\rho|$ exists only as a singular distribution, a windowing operation is needed in order to stabilize the computation. One can, e.g., think of the ramp filter response $h(l)$ as the limit of

$$h_\epsilon(l) = \begin{cases} +2/\epsilon^2, & \text{for } |l| < \epsilon \\ -2/l^2, & \text{for } |l| > \epsilon \end{cases} \tag{2.12}$$

as $\epsilon \to 0$. See [Horn, 1978] for detailed derivation.

Then in the 2D inverse reconstruction (Eqn. (2.8)), we have a two-step process: first "filter" the projection data in the radial direction (1D) by convolving with the ramp filter $h(l)$, then back project — i.e., take the integral over $\mathbf{S}^1$.

Chapter 3

Cone-beam Reconstruction: The Early Results

The 3D Radon inversion formula, Eqn. (2.10), is considered to be the cornerstone in the development of cone-beam reconstruction techniques. The inversion formulae given by Tuy [Tuy, 1983], Smith [Smith, 1985] and Grangeat [Grangeat, 1991] represent different ways of exploiting Eqn. (2.10) in the context of the cone-beam projective geometry — i.e., where Rf itself is actually *not* known. They share important similarities in that their implementations can be split into three phases, including two transformations and a backprojection:

- *Transformation of cone-beam projection data to a chosen intermediate function (e.g., the 1st-order radial derivative of Rf in Grangeat's formula);*
- *Transformation of the intermediate function to the 2nd radial derivative of Rf;*
- *Use of the Radon inversion formula Eqn. (2.10) to recover f.*

This chapter provides a thorough analysis on the theoretical results obtained by Tuy, Smith and Grangeat. Tuy and Smith's inversion formulae are introduced and briefly compared in section 3.1. We then give a new and simplified proof of Grangeat's *Fundamental Relation* in section 3.2, the emphasis being that this formulation is a result of the simple and nice differential property of the Radon transform. Our proof reveals more geometric

meaning underlying the *Fundamental Relation.* The study of mathematical equivalence of three inversion formulae, and extensions of these early results based on Fourier analysis are presented in section 3.3. Section 3.4 discusses the orbital condition for exact cone-beam reconstruction. We give this condition a new interpretation from the viewpoint of duality.

3.1 Revisiting Tuy and Smith

The density function f is compactly supported in $\mathbb{R}^3$. Let $\Omega = \text{supp}(f)$. Assume that the source orbit, parameterized by $\mathbf{\Phi}(\lambda)$ $(\lambda \in \Lambda)$, is a continuous and differentiable 3D curve, residing outside the convex hull of Ω. The cone-beam image obtained from a particular point source $\mathbf{\Phi}(\lambda)$ measures the half line integrals of attenuation along rays passing through $\mathbf{\Phi}(\lambda)$:

$$g(\lambda, \boldsymbol{\alpha}) = \int_0^{+\infty} f(\mathbf{\Phi}(\lambda) + t\boldsymbol{\alpha})\ dt, \quad \boldsymbol{\alpha} \in \mathbf{S}^2, \tag{3.1}$$

where $\boldsymbol{\alpha}$ is a vector belonging to the unit sphere $\mathbf{S}^2$ which we call the **projection sphere.** Note that both the projection sphere and the Radon sphere (or backprojection sphere) are viewed in the object space.

It is clear that cone-beam images do *not* directly capture the Radon transform since they contain integrals along *lines*, not over *planes* — if the lines were parallel, integrals over planes could be computed from the line integrals by one more integration. However, the lines *diverge* from the X-ray source in cone-beam imaging (see Fig. 3-1).

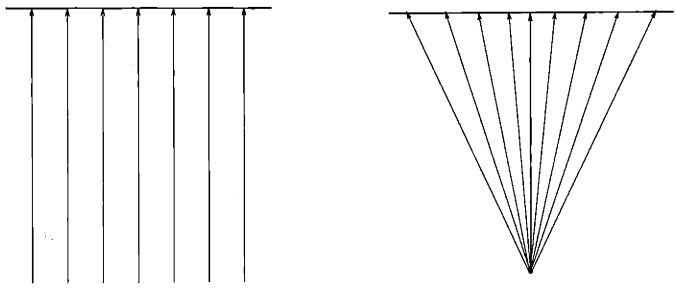

Figure 3-1: *Parallel-beam projection v.s. cone-beam projection (rays are restricted onto a thin slice).*

Tuy's and Smith's formulations are very similar in their initial use of the cone-beam data.

Both approaches extend the collection of line integrals of f, for a particular X-ray source position, homogeneously from the unit sphere into the whole 3D space, and then apply the 3D Fourier transform. The resulting Fourier transform serves as an intermediate function to link the cone-beam projection data to $R''f$.

The difference between the two approaches is in the form of the ray transform function: Tuy used the half line integral of f as the basis of extension, whereas Smith used the whole line integral.

- Tuy's ray transform is the half line integral, known as the **divergent ray transform**:

$$\boldsymbol{D}f(\lambda, \boldsymbol{\alpha}) := g_1(\lambda, \boldsymbol{\alpha}) = \int_0^{+\infty} f(\boldsymbol{\Phi}(\lambda) + t\boldsymbol{\alpha}) \; dt, \quad \boldsymbol{\alpha} \in \mathbf{S}^2. \tag{3.2}$$

- Smith's ray transform is the whole line integral, known as the **X-ray transform**:

$$\boldsymbol{X}f(\lambda, \boldsymbol{\alpha}) := g_2(\lambda, \boldsymbol{\alpha}) = \int_{-\infty}^{+\infty} f(\boldsymbol{\Phi}(\lambda) + t\boldsymbol{\alpha}) \; dt, \quad \boldsymbol{\alpha} \in \mathbf{S}^2. \tag{3.3}$$

For $\boldsymbol{\alpha} \in \mathbf{S}^2$ outside the collimator cone, the divergent ray transform $g_1(\lambda, \boldsymbol{\alpha})$ is considered to be zero. Since the angle between any two rays within a projection never exceeds π, we have, either $g_1(\lambda, \boldsymbol{\alpha}) = 0$ or $g_1(\lambda, -\boldsymbol{\alpha}) = 0$. As a result, the whole line integral $g_2(\lambda, \boldsymbol{\alpha}) = g_1(\lambda, \boldsymbol{\alpha}) + g_1(\lambda, -\boldsymbol{\alpha})$ is simply a symmetric extension of the half line integral g_1.

If $g(\boldsymbol{\alpha})$ is defined on the unit sphere $\mathbf{S}^2$, then the homogeneous extension $g^h(\boldsymbol{\alpha})$ of degree -1 to the 3D space is defined as follows:

$$g^h(r\boldsymbol{\alpha}) = \frac{1}{r} g(\boldsymbol{\alpha}). \tag{3.4}$$

Since the rate of decay is only in the magnitude of $|1/r|$, the Fourier transform of $g(\boldsymbol{\alpha})$ exists only as a distribution.

Let g_1^h and g_2^h be the homogeneous extension of g_1 and g_2 respectively with degree -1. Note that Eqn. (3.2) and (3.3) naturally allow for such extensions by relaxing $\boldsymbol{\alpha}$ from $\mathbf{S}^2$ to $\mathbb{R}^3$.

Tuy was the first to derive a cone-beam inversion formula for real-valued functions with projections from a bounded source curve. He obtained in [Tuy, 1983],

Theorem 3.1 *The density function f on Ω can be recovered from cone-beam data using*

$$f(\boldsymbol{x}) = \int_{\mathbf{S}^2} \frac{1}{2\pi i \boldsymbol{\Phi}'(\lambda)\cdot\boldsymbol{\beta}} \cdot \frac{\partial G_1(\lambda,\boldsymbol{\beta})}{\partial\lambda}\, d\boldsymbol{\beta}, \tag{3.5}$$

where $G_1(\lambda,\boldsymbol{\beta})$ is the 3D Fourier transform of $g_1^h(\lambda,\boldsymbol{\alpha}))$ restricted onto the unit sphere $\boldsymbol{\beta}\in\mathbf{S}^2$, and $\lambda\in\Lambda$ is a solution for $\boldsymbol{\Phi}(\lambda)\cdot\boldsymbol{\beta} = \boldsymbol{x}\cdot\boldsymbol{\beta}$ and $\boldsymbol{\Phi}'(\lambda)\cdot\boldsymbol{\beta}\neq 0$.

Eqn. (3.5) holds if the source orbit meets the following conditions:

(1) $\boldsymbol{\Phi}(\lambda)$ is outside $\Omega = \mathrm{supp}(f)$;

(2) $\boldsymbol{\Phi}(\lambda)$ is bounded, continuous and almost everywhere differentiable;

(3) For all $(\boldsymbol{x},\boldsymbol{\beta})\in\Omega\times\mathbf{S}^2$, there exists $\lambda\in\Lambda$ such that $\boldsymbol{\Phi}(\lambda)\cdot\boldsymbol{\beta} = \boldsymbol{x}\cdot\boldsymbol{\beta}$ and $\boldsymbol{\Phi}'(\lambda)\cdot\boldsymbol{\beta}\neq 0$.

In proving Theorem 3.1, Tuy used the following change of variables:

$$T: \begin{cases} \boldsymbol{x} = \boldsymbol{\Phi}(\lambda) + t\boldsymbol{\alpha}, & \boldsymbol{\alpha}\in\mathbb{R}^3,\ 0\le t\le\infty \\ \rho = \dfrac{1}{t}, & 0\le t\le\infty \end{cases}. \tag{3.6}$$

The Jacobian of the map T is $-\rho$. Therefore,

$$\begin{aligned} G_1(\lambda,\boldsymbol{\beta}) &= \int_{\mathbb{R}^3}\left(\int_0^\infty f(\boldsymbol{\Phi}(\lambda)+t\boldsymbol{\alpha})\ dt\right) e^{-2\pi i\boldsymbol{\alpha}\cdot\boldsymbol{\beta}}\, d\boldsymbol{\alpha} \\ &= \int_{\mathbb{R}^3}\int_0^\infty \rho f(\boldsymbol{x}) e^{-2\pi i\rho(\boldsymbol{x}-\boldsymbol{\Phi}(\lambda))\cdot\boldsymbol{\beta}}\, d\rho\, d\boldsymbol{x} \\ &= \int_0^\infty \rho e^{2\pi i\rho\boldsymbol{\Phi}(\lambda)\cdot\boldsymbol{\beta}}\left(\int_{\mathbb{R}^3} f(\boldsymbol{x}) e^{-2\pi i\rho\boldsymbol{x}\cdot\boldsymbol{\beta}}\, d\boldsymbol{x}\right) d\rho \\ &= \int_0^\infty \rho F_{\boldsymbol{x}\to\boldsymbol{\xi}}(\rho\boldsymbol{\beta}) e^{2\pi i\rho\boldsymbol{\Phi}(\lambda)\cdot\boldsymbol{\beta}}\, d\rho. \end{aligned} \tag{3.7}$$

Then Eqn. (3.5) can be verified by plugging in Eqn. (3.7) and comparing the result to the inversion formula for the Fourier transform in spherical coordinates:

$$f(\boldsymbol{x}) = \int_{\mathbf{S}^2}\left(\int_0^\infty \rho^2 F_{\boldsymbol{x}\to\boldsymbol{\xi}}(\rho\boldsymbol{\beta}) e^{2i\pi\rho\boldsymbol{\beta}\cdot\boldsymbol{x}}\, d\rho\right) d\boldsymbol{\beta}. \tag{3.8}$$

Clearly, to use this result, at least one solution $\lambda\in\Lambda$ for $\boldsymbol{\Phi}(\lambda)\cdot\boldsymbol{\beta} = \boldsymbol{x}\cdot\boldsymbol{\beta}$ and $\boldsymbol{\Phi}'(\lambda)\cdot\boldsymbol{\beta}\neq 0$ needs to be found for all (or almost all) $(\boldsymbol{x},\boldsymbol{\beta})\in\Omega\times\mathbf{S}^2$. Condition $\boldsymbol{\Phi}'(\lambda)\cdot\boldsymbol{\beta}\neq 0$

eliminates the case of tangential intersection between a plane passing through supp(f) with the source orbit. Finch proved that these conditions are also necessary for stable reconstruction [Finch, 1985].

Because Tuy's inverse is implicit with respect to the source curve parameter λ, a practical implementation is not immediately available.

Smith used a similar function — the 3D Fourier transform of g_2^h with respect to $\boldsymbol{\alpha}$, denoted by $G_2(\lambda, \boldsymbol{\beta})$ (restricted onto the unit sphere $\boldsymbol{\beta} \in \mathbf{S}^2$). He found the following connection: $G_2(\lambda, \boldsymbol{\beta})$ is proportional to the Hilbert transform $\mathcal{H}$ of the radial derivative $R'f(l, \boldsymbol{\beta}) \mid_{l=\boldsymbol{\Phi}(\lambda)\cdot\boldsymbol{\beta}}$.

The Hilbert transform of a function can be written as a convolution with $1/(\pi s)$ (see Eqn. (2.5)). The 1D Fourier Transform of this convolution corresponds to multiplication with $(1/i)\mathrm{sgn}\rho$, where ρ is the radial frequency. The Hilbert transform appears also in the simpler 2D case.

The derivative in the radial direction corresponds to multiplication by $i\rho$ in the transform domain. The composition of the two operations then corresponds to multiplication by $i\rho(1/i)\mathrm{sgn}(\rho) = |\rho|$. The inverse Fourier transform of this (which exists only as a distribution) is the ramp filter familiar from 2D reconstruction (given in Eqn. (2.12)).

If we apply the ramp filter to G_2 we obtain $R''f$, accordingly, the 3D Radon inversion formula can be evoked. In [Smith, 1985], Smith obtained

Theorem 3.2 *The density function f on Ω can be recovered from cone-beam data using*

$$f(\boldsymbol{x}) = -\frac{1}{8\pi^3} \int_{\mathbf{S}^2} \Big(h(l) \otimes F(l, \boldsymbol{\beta}) \Big)\, d\boldsymbol{\beta}, \tag{3.9}$$

where $\otimes$ denotes convolution, $h(l)$ is the ramp filter response, and $F(l, \boldsymbol{\beta}) = G_2(\lambda, \boldsymbol{\beta})$ with $l = \boldsymbol{\Phi}(\lambda) \cdot \boldsymbol{\beta} = \boldsymbol{x} \cdot \boldsymbol{\beta}$.

Again, to make this work, for all (or almost all) $(\boldsymbol{x}, \boldsymbol{\beta}) \in \Omega \times \mathbf{S}^2$, at least one solution $\lambda \in \Lambda$ needs to be found such that $\boldsymbol{\Phi}(\lambda) \cdot \boldsymbol{\beta} = \boldsymbol{x} \cdot \boldsymbol{\beta}$. As in Tuy's case, Smith's inversion formula is implicit with respect to λ.

3.2 Grangeat's *Fundamental Relation* — A Simplified Proof

The intuitive key in Grangeat's inverse formulation is that the first radial derivative of the Radon transforms can be computed from cone-beam data. If the rays were parallel, the situation would be much simpler, since the Radon transforms over 2D planes could be obtained via 1D integrals. However, in the cone-beam case, rays diverge from the point source and the Radon transform itself cannot be recovered.

According to Grangeat's *Fundamental Relation*, each slice of fan beams, and its adjacent slices *within* a projection, supplies the first radial derivative of the Radon transform.

A typical fan-beam slice is shown in Fig. (3-2).

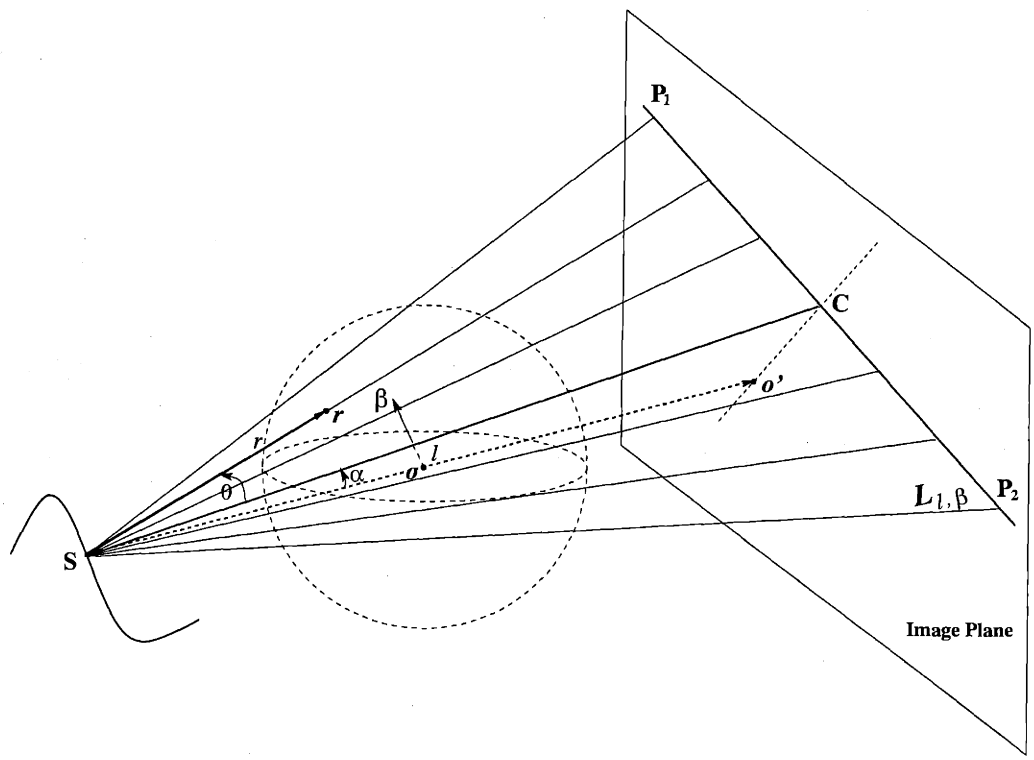

Figure 3-2: *Illustration of a fan-beam slice intersecting with the image plane.*

In Fig. (2-4), a Radon plane intersecting the support of f is denoted by $\boldsymbol{L}_{l,\beta}$. Denote by P_1P_2 the intersection line between $\boldsymbol{L}_{l,\beta}$ and the image plane. Denote by α the angle between $\boldsymbol{L}_{l,\beta}$ and the principal direction which may go by the name the **angle of the slice** (it is a term for convenience). Let the **central ray** be the shortest line on $\boldsymbol{L}_{l,\beta}$ from the

point source to the detector plane, denoted by SC. Note that SC is perpendicular to P_1P_2.

Because the fan beams restricted onto the plane $\boldsymbol{L}_{l,\beta}$ all meet at the source, it seems natural to use polar coordinates on this plane, with the origin placed at the X-ray source and the axis aligned with the central ray. Denote by r and θ the radial and angular parameters respectively in this polar coordinates.

Then, Grangeat's **Fundamental Relation** [Grangeat, 1991] can be re-stated as

Theorem 3.3 *The first radial derivative of the Radon transform, $R'f$, can be computed from cone-beam projection data using*

$$\frac{\partial Rf(l,\beta)}{\partial l} = -\frac{\partial}{\partial \alpha}\left\{ \int \frac{1}{\cos\theta} \int f(\boldsymbol{r})\, dr\, d\theta \right\}, \tag{3.10}$$

where the double integral is performed on the plane $\boldsymbol{L}_{l,\beta}$.

Note that the inner integral $\int f(\boldsymbol{r})\, dr$, for some fixed θ, represents an X-ray projection in polar coordinates on the Radon plane $\boldsymbol{L}_{l,\beta}$ — this is a measurement available from the cone-beam image.

Proof: We shall slightly change our viewing angle and set up local Cartesian coordinates as follows:

$$\begin{cases} \boldsymbol{y}' &= -\dfrac{\boldsymbol{\Phi}(\lambda)}{|\boldsymbol{\Phi}(\lambda)|} \\ \boldsymbol{x}' &= \boldsymbol{y}' \times \boldsymbol{\beta} \\ \boldsymbol{z}' &= \boldsymbol{x}' \times \boldsymbol{y}' \end{cases} \tag{3.11}$$

with the origin at $\boldsymbol{\Phi}(\lambda)$ (Fig. (3-3)). Note that the principal direction is aligned with the y-axis but runs in the opposite direction.

This coordinate system is exceptionally convenient for expressing an arbitrary point $\boldsymbol{r} \in \boldsymbol{L}_{l,\beta}$ in terms of the distance along the ray from the source, r, and two angles, θ and α:

$$\boldsymbol{r} = < r\sin\theta, r\cos\theta\cos\alpha, r\cos\theta\sin\alpha > . \tag{3.12}$$

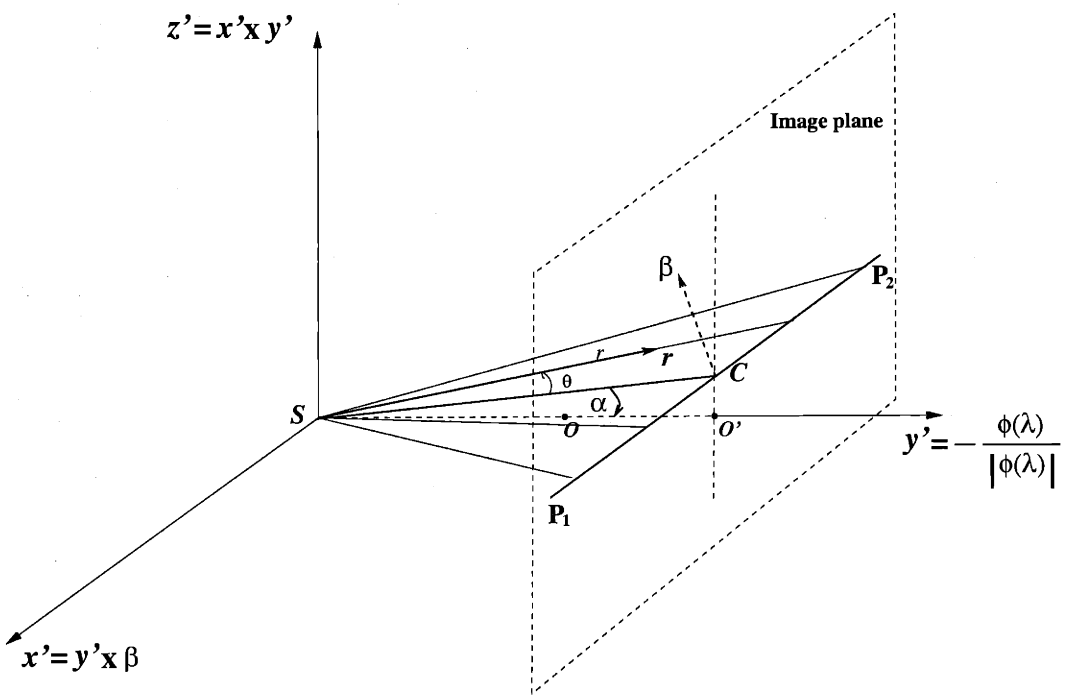

Figure 3-3: *A local coordinate is intentionally set up for a particular fan-beam slice* $L_{l,\beta}$. *The principal direction is aligned with the y-axis.*

In this coordinate system, the plane normal β has the form

$$\beta \;=\; < 0, -\sin\alpha, \cos\alpha > . \tag{3.13}$$

Integrating the inner integral, $\int f(\boldsymbol{r})\, dr$, by part and applying zero boundary condition, we get

$$\begin{aligned} \int f(\boldsymbol{r})\, dr &= -\int r \nabla f \cdot \frac{\partial \boldsymbol{r}}{\partial r}\, dr \\ &= -\int r(\sin\theta f_x + \cos\theta\cos\alpha f_y + \cos\theta\sin\alpha f_z)\, dr. \end{aligned} \tag{3.14}$$

Using this result, we compute

$$\begin{aligned} \frac{\partial}{\partial\alpha}\Big\{\int \frac{1}{\cos\theta}\int f(\boldsymbol{r})\, dr\, d\theta\Big\} &= \int\int r\big(f_y\sin\alpha - f_z\cos\alpha\big)\, dr\, d\theta \\ &= -\int\int r\Big(\boldsymbol{\beta}\cdot\nabla f\Big)\, dr\, d\theta. \end{aligned} \tag{3.15}$$

Here, $\int\int r\Big(\boldsymbol{\beta}\cdot\nabla f\Big)\,dr\,d\theta$ can be easily recognized as the Radon transform of $\boldsymbol{\beta}\cdot\nabla f$ in the polar form. By the differential property of the Radon transform (Eqn. (2.4))

$$-R\Big\{\boldsymbol{\beta}\cdot\nabla f\Big\} = -\boldsymbol{\beta}\cdot\boldsymbol{\beta}\frac{\partial Rf(l,\boldsymbol{\beta})}{\partial l} = -\frac{\partial Rf(l,\boldsymbol{\beta})}{\partial l}. \tag{3.16}$$

The last equality holds because $\boldsymbol{\beta}\cdot\boldsymbol{\beta}=1$. It leads us to the *Fundamental Relation.* ∎

The ray transform used in Grangeat's formula can be expressed as

$$\boldsymbol{P}f(\lambda,r\boldsymbol{\alpha}) := g_3(\lambda,r\boldsymbol{\alpha}) = \int_0^{+\infty} f(\boldsymbol{\Phi}(\lambda)+t\boldsymbol{\alpha})\,dt, \quad \boldsymbol{\alpha}\in\mathbf{S}^2,\ r\in\mathbb{R}, \tag{3.17}$$

which is a homogeneous function of degree 0. What Eqn. (3.17) does is projecting the image of the divergent ray transform $g_1(\lambda,\boldsymbol{\alpha})$ from the projection sphere to the image plane (see Fig. 3-4).

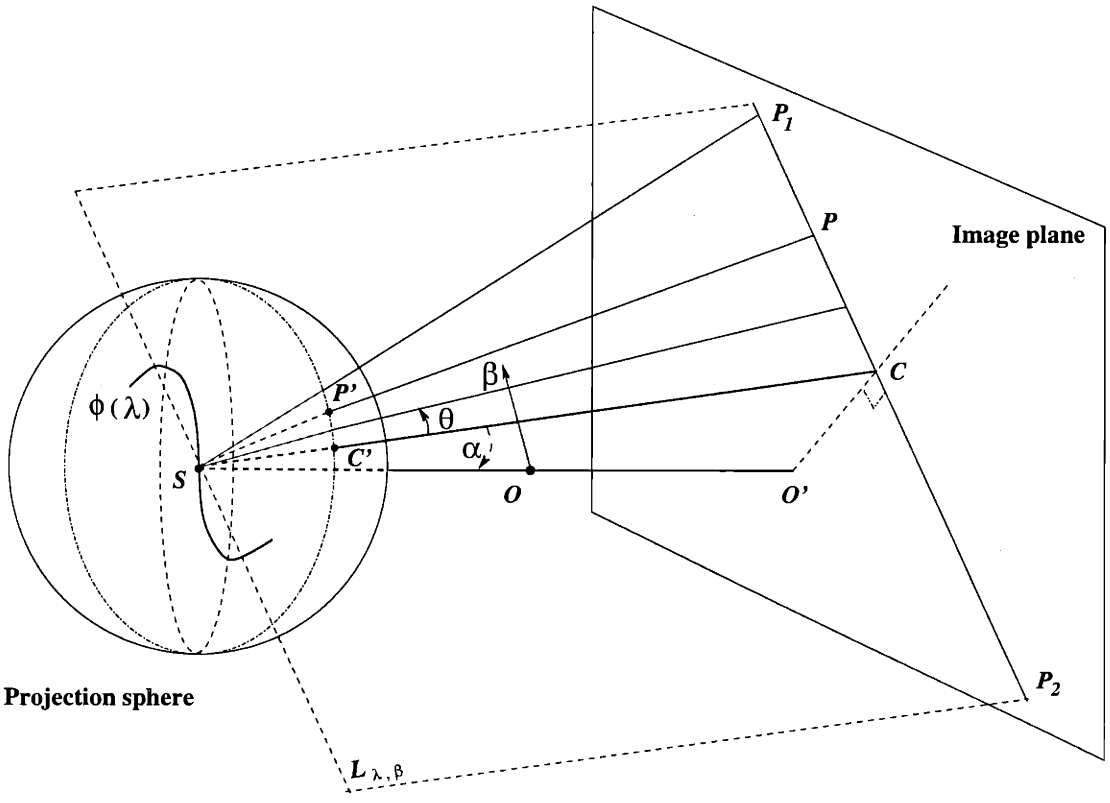

Figure 3-4: *Ray transform function g_3 is the projection of g_1 onto the image plane.*

The ray sampling density on the projection sphere is typically uniform, hence, on each intersection line between a Radon plane and a image plane, the ray sampling density varies proportionally to the *cos* of the angle between a particular ray and the central ray (sampling is finer near the central ray). The weighting factor, $1/(\cos\theta)$, in Eqn. (3.10) is therefore used to counter-balance the ray sampling density. As a result, the weighted line integral of the density integrals on a given Radon plane reflects the mean value of the divergent ray transforms on that plane.

We are able to show that the *Fundamental Relation* is a result of the differential property of the Radon transform. Our proof also reveals the geometric significance of the varying angle of the slice, α. This angle α is an intuitive link between the coordinates in the projection reference frame and the coordinates in the Radon space. For $\forall\boldsymbol{\beta} \in \mathbf{S}^2$, a simple relationship holds:

$$l = |OS| \sin\alpha, \tag{3.18}$$

where l is radial parameter of the Radon plane, and $|OS|$ is the distance from the source to the origin (see Fig. 3-5).

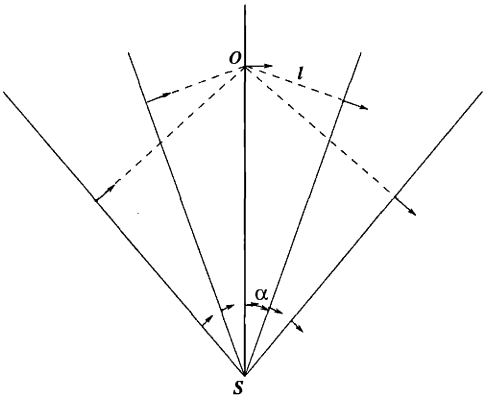

Figure 3-5: *Relation of the radial parameter, l, and the angle of the slice, α.*

As a limiting case, where X-ray source is put infinitely far, the parallel projection corresponds to $\theta = 0$ and $\alpha = 0$ (see Fig. 3-6). Accordingly, the parallel projection can be well suited into the *Fundamental Relation* by setting $\cos\theta = 1$ and $\dfrac{\partial}{\partial\alpha} = \dfrac{\partial}{\partial l}$ in Eqn. (3.10). Note that $\cos\theta = 1$ reflects the uniform ray sampling in the parallel projection scheme.

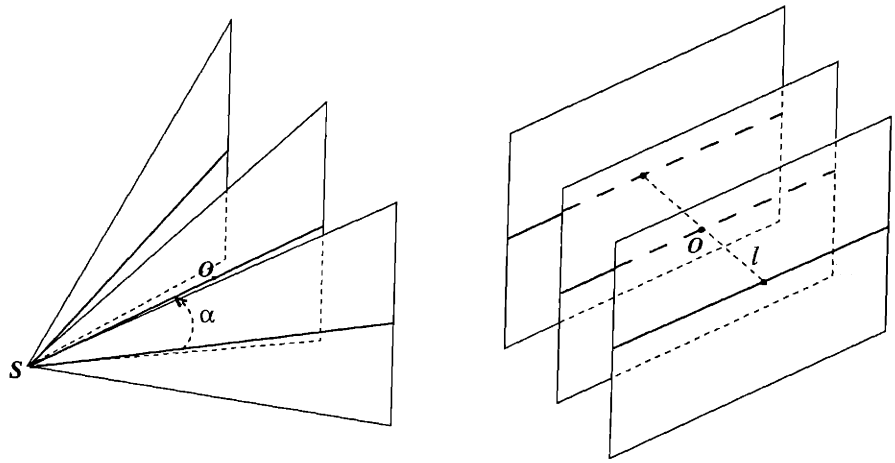

Figure 3-6: *Parallel-beam projection as a limiting case of cone-beam projection.*

The distance from the source to the image plane is fixed for each projection, denoted by $|O'S|$ (O' is the projection of the origin O from the point source S). Let s be the radial distance of the intersection line on the image plane from the image center O'. It is easy to verify that

$$s = |O'S| \tan \alpha. \tag{3.19}$$

Therefore, the partial derivative with respect to α in Eqn. (3.10) can be evaluated through the radial derivative of the weighted line integrals on the image plane [Grangeat, 1991]:

$$\frac{\partial}{\partial \alpha} = \frac{|O'S|}{(1 - \tan^2 \alpha)} \frac{\partial}{\partial s}. \tag{3.20}$$

The $2nd$-order radial derivative of the Radon transform $R''f$ is uniquely determined by the scalar field $R'f$. And from $R''f$ we can find f using 3D backprojection (Eqn. (2.10)).

An apparent advantage of Grangeat's formula lies in its *directness* in relating itself to the Radon inversion formula and its operational simplicity. From each cone-beam projection, a set of $1st$-order radial derivative of the Radon transforms can be easily computed by differentiating over a set of fan-beam slices. Because derivative acts locally, Grangeat's formula prevails in locality as well. However, this locality feature in Grangeat's formula can not be used too naively, since the rays penetrating the object are almost always contaminated by

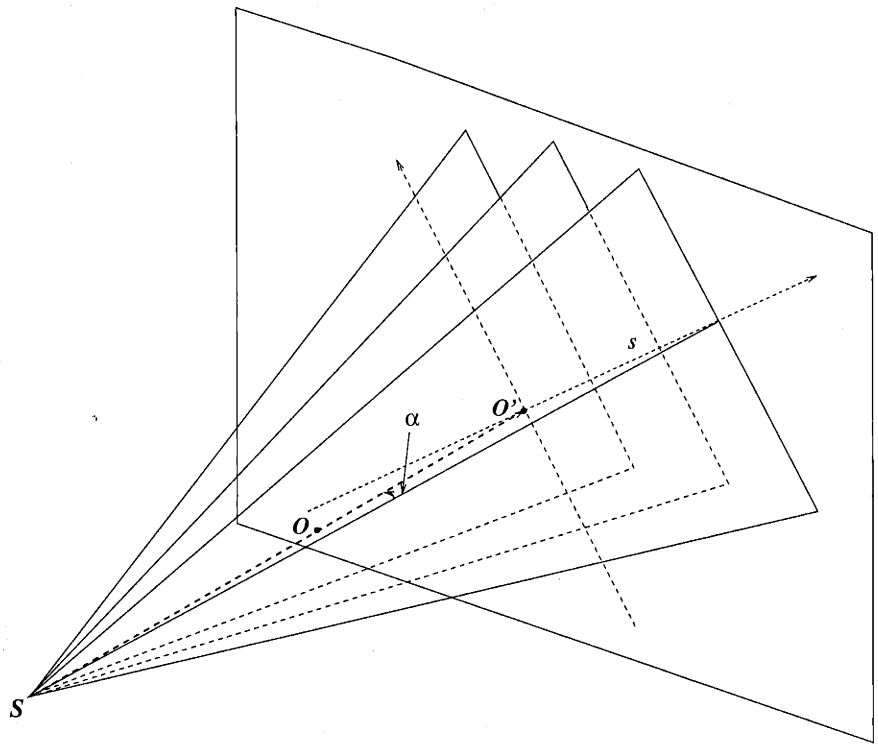

Figure 3-7: *Derivative with respect to α corresponds to derivative with respect to the radial distance on the image plane.*

attenuation outside the ROI (region of interest), as a result, locality can only be achieved in a limited sense. On the other hand, a successful application of Grangeat's formula can be found in the local scans of a long object via longitudinal data truncation.

Grangeat's formula provides the first radial derivative of the Radon transform. However, the link between the first derivative $R'f$ and the second derivative $R''f$ is more *elusive* than it *looks*, and indeed there is a misconception here that is more of a superficial misunderstanding. To explain this, we notice that a *coordinate* is needed to compute $R''f$ from $R'f$. We have not yet found a natural coordinate to accomplish such a task — the Radon space is just not a usual space we are familiar with. A common practice in current cone-beam reconstruction algorithms makes use of the spherical coordinates in the warped space $\tilde{\mathbb{R}}^3$ (it was introduced in section 2.1). In these methods, the first radial derivatives of the Radon transform obtained from the cone-beam measurements are resampled and interpolated along a set of radial directions, then finite difference is applied to compute the second derivative.

A clear sign of its incorrect sampling scheme is the singularity at the origin, where, the Radon transform and its derivatives are not meaningful because the direction of the plane passing by the origin can not even be recovered. Besides, as we have mentioned in section 2.1, the geometric relationships in the Radon space $\mathbf{P}^3$ are not correctly duplicated by $\tilde{\mathbb{R}}^3$. We are actually disoriented in the Radon space under Euclidean influence. To correct this, we need to further understand the Radon space geometry in connection with the cone-beam geometry. We will take time to do this in the next chapter.

One obvious but also important observation is that the backprojection is common to all three inversion methods derived by Tuy, Smith and Grangeat (Eqn. (3.5), (3.9) and (3.10)). It turns out, as will be deliberated in section 3.3.2, that the odd part of Tuy's intermediate function G_1 is related to Grangeat's intermediate function $Rf'(l,\beta)$, the $1st$-order radial derivative of the Radon transform, and the even part of G_1 is linked to Smith's intermediate function G_2, the Hilbert transform of $Rf'(l,\beta)$. The striking similarity among three inversion formulae in terms of the backprojection is because they are all but disguised faces of the 3D Radon inverse (Eqn. (2.10)).

It is clear that these three inversion formulae do not immediately provide efficient reconstruction algorithms. The most expensive operation — differential-backprojection (or filtered-backprojection in Smith's case), which is performed in the projective Radon space, has implicit dependence on the source curve parameter λ. In this sense, the backprojection is a *problematic issue* common to all three inversion methods.

3.3 Algebraic Varieties in Cone-beam Reconstruction

In this section, we seek out for the relationships of Tuy, Smith and Grangeat's cone-beam inversion formulae. Our aims are:

- To make it conceptually easy to take: why we have not just one, but three cone-beam inversion formulae? Where do they differ? How do they connect?
- To reveal the significance of the homogeneous space within each cone-beam projection, as well as the algebraic varieties and geometric hierarchies inherent in this subsystem.

- To demonstrate the strong connection between the Fourier transform and the Radon transform, and similar connections between their derivatives as well.

- To reveal the duality principle in the subsystem.

3.3.1 The Homogeneous Space

Each cone-beam projection consists of rays emitting from a point source. The pencil of divergent rays form a 2D projective space with its projection center at the X-ray source. This space is equipped with the following equivalence relation

$$\boldsymbol{\alpha} \sim r\boldsymbol{\alpha} \quad \text{for } r \neq 0. \tag{3.21}$$

It induces homogeneous coordinates, in which, multiplying the coordinates of a point by a nonzero number does not change its position. The projective space is also known to mathematicians as the homogeneous space. This latter one will be used consistently with our discussion of the homogeneous functions defined on the same space. Denote by H_λ the homogeneous space attached to the X-ray source at $\boldsymbol{\Phi}(\lambda)$ ($\lambda \in \Lambda$), where Λ is the indexing set.

In the homogeneous space H_λ, various inversion formulae take their initial form. Already, we have seen three ray transform functions defined on H_λ, namely g_1^h, g_2^h, and g_3 with homogeneous degree -1, -1 and 0 respectively. The integral transform of g_1^h, g_2^h and g_3 then lead us to some intermediate functions in the Radon transform domain and can be inverted through the 3D Radon inversion formula after all the projection data has been collected and transformed into the Radon space. In this sense, each cone-beam projection subsystem plays a significant role in cone-beam reconstruction. While the main source of variations in algebra can be attributed to the homogeneous coordinates *within* each cone-beam projection.

The algebra attached to the homogeneous space is rich and variant. However, it is a deeply involved subject and is not the main effort of this thesis. We will only try to gain some fundamental understanding of the algebraic varieties related to our cone-beam problem in

the coming discussion.

3.3.2 Differential Form

This section is intended to show, using Fourier analysis, how Tuy, Smith and Grangeat's inversion formulae are connected by the differential form of the Radon transform. The basic tools used are the *derivative property* of the Fourier transform as well as the *Central slice theorem* of the Radon transform (see section 2.2). The later relates the Radon transform to the Fourier transform.

We shall pay attention to the *even* and *odd* game played between G_1, G_2 and the Radon transform derivative. As a reminder, G_1 and G_2 are the Fourier transform of the divergent ray transform g_1^h in the 3D space and its symmetric counterpart g_2^h respectively. We shall also pay attention to how each Fourier transform derivative parallels with a derivative of the Radon transform.

We start with the more general nD case, since the projective space $\mathbf{P}^n$ nestles a chain of projective subspace with lower dimensions, i.e., $\mathbf{P}^{n-1}, \mathbf{P}^{n-2}, \cdots, \mathbf{P}^1$. Note that the Radon space, $\mathbf{P}^n$, is at the top of this dimensional hierarchy, and the fan-beam projection, corresponding to a 1D projective space, is located down at the bottom. By understanding the general context of reconstruction in nD space, we are not only in a position to see the inner build-ups of the nD Radon inverse, but also be able to compare 3D cone-beam reconstruction with 2D fan-beam reconstruction, so that analogies can be drawn and knowledge of old and new can be exchanged.

In $\mathbb{R}^n$, the homogeneous extension (with degree -1) of the divergent ray transform $g_1(\lambda, \boldsymbol{\alpha})$ can be expressed as

$$g_1^h(\lambda, \boldsymbol{\alpha}) = \int_0^\infty f(\boldsymbol{\Phi}(\lambda) + t\boldsymbol{\alpha})\, dt, \quad \boldsymbol{\alpha} \in \mathbb{R}^n, \tag{3.22}$$

where $\boldsymbol{\alpha}$ is a vector in $\mathbb{R}^n$. The X-ray transform is the symmetric extension of the divergent ray transform, hence

$$g_2^h(\lambda, \boldsymbol{\alpha}) = g_1^h(\lambda, \boldsymbol{\alpha}) + g_1^h(\lambda, -\boldsymbol{\alpha}), \quad \boldsymbol{\alpha} \in \mathbb{R}^n. \tag{3.23}$$

Denote G_1 and G_2 as the nD Fourier transform of g_1^h and g_2^h respectively. Then,

$$\begin{aligned} G_1(\lambda,\boldsymbol{\beta}) &= \int_{\mathbb{R}^n} g_1(\lambda,\alpha) e^{-2\pi i \boldsymbol{\alpha}\cdot\boldsymbol{\beta}}\, d\boldsymbol{\alpha} \\ &= \int_{\mathbb{R}^n}\int_0^\infty f(\boldsymbol{\Phi}(\lambda)+t\boldsymbol{\alpha}) e^{-2\pi i \boldsymbol{\alpha}\cdot\boldsymbol{\beta}}\, dt\, d\boldsymbol{\alpha} \end{aligned} \tag{3.24}$$

and, by the scaling law of the Fourier transform, we have for G_2:

$$G_2(\lambda,\boldsymbol{\beta}) = G_1(\lambda,\boldsymbol{\beta}) + G_1(\lambda,-\boldsymbol{\beta}). \tag{3.25}$$

We mimic Tuy [Tuy, 1983] in choosing the following mapping

$$T: \begin{cases} \boldsymbol{x} = \boldsymbol{\Phi}(\lambda)+t\boldsymbol{\alpha}, & \boldsymbol{\alpha}\in\mathbb{R}^n,\ 0\le t<\infty \\ \rho = \dfrac{1}{t}, & 0\le t<\infty \end{cases}. \tag{3.26}$$

Now, $\boldsymbol{\alpha}\in\mathbb{R}^n$ is a high dimensional vector so the Jacobian of T becomes $-\rho^{n-2}$. Via the change of variables in Eqn. (3.24) we obtain

$$\begin{aligned} G_1(\lambda,\boldsymbol{\beta}) &= \int_{\mathbb{R}^n}\int_0^\infty \rho^{n-2} f(\boldsymbol{x}) e^{-2\pi i\rho(\boldsymbol{x}-\boldsymbol{\Phi}(\lambda))\cdot\boldsymbol{\beta}}\, d\rho\, d\boldsymbol{x} \\ &= \int_0^\infty \rho^{n-2} e^{2\pi i\rho\boldsymbol{\Phi}(\lambda)\cdot\boldsymbol{\beta}} \int_{\mathbb{R}^n} f(\boldsymbol{x}) e^{-2\pi i\rho\boldsymbol{x}\cdot\boldsymbol{\beta}}\, d\boldsymbol{x}\, d\rho \\ &= \int_0^\infty \rho^{n-2} F_{\boldsymbol{x}\to\boldsymbol{\xi}}(\rho\boldsymbol{\beta}) e^{2\pi i\rho\boldsymbol{\Phi}(\lambda)\cdot\boldsymbol{\beta}}\, d\rho. \end{aligned} \tag{3.27}$$

For notational convenience, we will sometimes denote $F_{\boldsymbol{x}\to\boldsymbol{\xi}}$ by $F_{\boldsymbol{x}}$. Plugging Eqn. (3.27) into Eqn. (3.25) which is G_2, we obtain the *even* part of G_1 (with respect to $\boldsymbol{\beta}$),

$$\begin{aligned} &G_1(\lambda,\boldsymbol{\beta}) + G_1(\lambda,-\boldsymbol{\beta}) = \\ &\qquad \int_0^\infty \rho^{n-2} F_{\boldsymbol{x}}(\rho\boldsymbol{\beta}) e^{2\pi i\rho\boldsymbol{\Phi}(\lambda)\cdot\boldsymbol{\beta}}\, d\rho + \int_0^\infty \rho^{n-2} F_{\boldsymbol{x}}(-\rho\boldsymbol{\beta}) e^{-2\pi i\rho\boldsymbol{\Phi}(\lambda)\cdot\boldsymbol{\beta}}\, d\rho. \end{aligned} \tag{3.28}$$

The odd part of G_1 is

$$\begin{aligned} &G_1(\lambda,\boldsymbol{\beta}) - G_1(\lambda,-\boldsymbol{\beta}) = \\ &\qquad \int_0^\infty \rho^{n-2} F_{\boldsymbol{x}}(\rho\boldsymbol{\beta}) e^{2\pi i\rho\boldsymbol{\Phi}(\lambda)\cdot\boldsymbol{\beta}}\, d\rho - \int_0^\infty \rho^{n-2} F_{\boldsymbol{x}}(-\rho\boldsymbol{\beta}) e^{-2\pi i\rho\boldsymbol{\Phi}(\lambda)\cdot\boldsymbol{\beta}}\, d\rho. \end{aligned} \tag{3.29}$$

We are now ready to prove the following:

Theorem 3.4 *G_1, G_2 and the Radon transform are related by*

$$\left.\frac{\partial^{n-2} Rf(l,\boldsymbol{\beta})}{\partial l^{n-2}}\right|_{l=\boldsymbol{\Phi}(\lambda)\cdot\boldsymbol{\beta}} = \begin{cases} \frac{(2\pi i)^{n-2}}{2\pi}\Big(G_1(\lambda,\boldsymbol{\beta}) + G_1(\lambda,-\boldsymbol{\beta})\Big) \\ \quad = \frac{(2\pi i)^{n-2}}{2\pi} G_2(\lambda,\boldsymbol{\beta}) \ , & n \text{ even} \\ \frac{(2\pi i)^{n-2}}{2\pi}\Big(G_1(\lambda,\boldsymbol{\beta}) - G_1(\lambda,-\boldsymbol{\beta})\Big) \ , & n \text{ odd} \end{cases} \tag{3.30}$$

$$\mathcal{H}_l\left\{\frac{\partial^{n-2} Rf(l,\boldsymbol{\beta})}{\partial l^{n-2}}\right\}\Bigg|_{l=\boldsymbol{\Phi}(\lambda)\cdot\boldsymbol{\beta}} = \begin{cases} (2\pi i)^{n-3}\Big(G_1(\lambda,\boldsymbol{\beta}) + G_1(\lambda,-\boldsymbol{\beta})\Big) \\ \quad = (2\pi i)^{n-3} G_2(\lambda,\boldsymbol{\beta}) \ , & n \text{ odd} \end{cases} \tag{3.31}$$

Proof: We have, from the *Central Slice Theorem* of the Radon transform

$$\int_{-\infty}^{+\infty} \rho^{n-2} F_{\boldsymbol{x}}(\rho\boldsymbol{\beta}) e^{2\pi i\rho\boldsymbol{\Phi}(\lambda)\cdot\boldsymbol{\beta}} \mathrm{d}\rho = \int_{-\infty}^{+\infty} \rho^{n-2} F_{l\to\rho}\Big\{Rf(l,\boldsymbol{\beta})\Big\} e^{2\pi i\rho\boldsymbol{\Phi}(\lambda)\cdot\boldsymbol{\beta}} \mathrm{d}\rho. \tag{3.32}$$

Using the the derivative property of the Fourier transform, we get

$$\frac{(2\pi i)^{n-2}}{2\pi}\int_{-\infty}^{+\infty} \rho^{n-2} F_{l\to\rho}\Big\{Rf(l,\boldsymbol{\beta})\Big\} e^{2\pi i\rho\boldsymbol{\Phi}(\lambda)\cdot\boldsymbol{\beta}} \mathrm{d}\rho = \left.\frac{\partial^{n-2}}{\partial l^{n-2}} Rf(l,\boldsymbol{\beta})\right|_{l=\boldsymbol{\Phi}(\lambda)\cdot\boldsymbol{\beta}}. \tag{3.33}$$

Combining (3.32) and (3.33) yields

$$\frac{(2\pi i)^{n-2}}{2\pi}\int_{-\infty}^{+\infty} \rho^{n-2} F_{\boldsymbol{x}}(\rho\boldsymbol{\beta}) e^{2\pi i\rho\boldsymbol{\Phi}(\lambda)\cdot\boldsymbol{\beta}} \mathrm{d}\rho = \left.\frac{\partial^{n-2}}{\partial l^{n-2}} Rf(l,\boldsymbol{\beta})\right|_{l=\boldsymbol{\Phi}(\lambda)\cdot\boldsymbol{\beta}}. \tag{3.34}$$

Briefly recall the discussion in section 2.3, the Hilbert transform in Fourier language corresponds to multiplying the radial frequency ρ by $(1/i)\mathrm{sgn}(\rho)$. Hence, when n is odd, changing ρ^{n-2} in Eqn. (3.34) to $|\rho|^{n-2}$ leads to

$$\frac{(2\pi i)^{n-2}}{2\pi i}\int_{-\infty}^{+\infty} |\rho|^{n-2} F_{\boldsymbol{x}}(\rho\boldsymbol{\beta}) e^{2\pi i\rho\boldsymbol{\Phi}(\lambda)\cdot\boldsymbol{\beta}} \mathrm{d}\rho = \mathcal{H}_l\left\{\frac{\partial^{n-2} Rf(l,\boldsymbol{\beta})}{\partial l^{n-2}}\right\}\Bigg|_{l=\boldsymbol{\Phi}(\lambda)\cdot\boldsymbol{\beta}}. \tag{3.35}$$

When n is even, $|\rho|^{n-2} = \rho^{n-2}$ so the result is the same.

Comparing equations (3.34) and (3.35) with (3.28) and (3.29), we notice that the major discrepancies lie in the forms of the integral range. So we rewrite the second term in Eqn. (3.28) and (3.29) (which is $G_1(\lambda, -\beta)$) by a change of variable from ρ to $-\rho$:

$$\int_0^\infty \rho^{n-2} F_{\boldsymbol{x}}(-\rho\boldsymbol{\beta}) e^{-2\pi i \rho \Phi(\lambda)\cdot\boldsymbol{\beta}}\, d\rho = \int_{-\infty}^0 (-\rho)^{n-2} F_{\boldsymbol{x}}(\rho\boldsymbol{\beta}) e^{2\pi i \rho \Phi(\lambda)\cdot\boldsymbol{\beta}}\, d\rho \tag{3.36}$$

Note that $(-\rho)^{n-2}$ in the above equation can be written as ρ^{n-2} for even n and $|\rho|^{n-2}$ for odd n. Plugging Eqn. (3.36) back into the *even* and *odd* equations (3.28) and (3.29) and comparing the results with (3.34) and (3.35), it yields (3.30) and (3.31). ∎

All is satisfying after this even-or-odd game is complete. There is a difference between the even and odd dimensions. To make the even and odd rules more straight, we draw the following diagram:

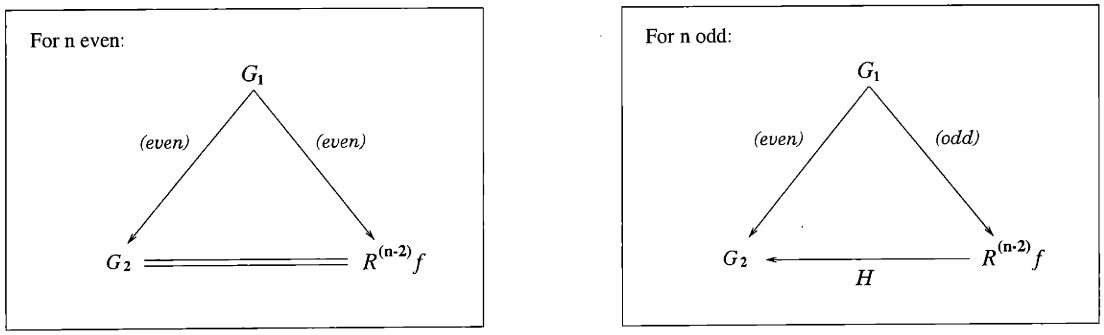

Figure 3-8: *Relationships between the Fourier transform of the divergent ray transform, X-ray transform and the Radon transform derivatives.*

In the case of $n = 3$, the odd part of G_1 goes to $R'f$, the first radial derivative of the Radon transform, while the even part of G_1 goes to G_2, the Hilbert transform of $R'f$. Tuy, Smith and Grangeat start with three different ray transform functions, now they meet, for the first time, at this triangle. Recall from the proof of Theorem 3.4, it is easy to understand that they are connected by the nice and simple differential properties of the Fourier transform and the Radon transform. From here, Tuy, Smith and Grangeat set foot on separate paths again to complete their reconstructions. Our intention in the next chapter is to start with this triangle meeting and develop a common framework to carry Tuy, Smith and Grangeat's

immediate functions, G_1, G_2 and $R'f$, towards the final reconstruction.

In the general context, the n-dimensional space, we observe that the homogeneous space spanned by the divergent rays within each cone-beam projection, which is a $(n-1)$D projective space, supplies the $(n-2)th$ differential form of the Radon transform. The ladder, certainly a mysterious medium in this dimensional hierarchy, is ρ^{n-2} from the Jacobian of the mapping T! At the bottom level, we have the familiar 2D fan-beam case (1D projective space). And at the top is the whole Radon space $\mathbf{P}^n$. It is observed that the dimensional hierarchy inherent in the nD projective space is highly dependent on its foundational 1D space. It should not be a surprise that the non-local character in 2D reconstruction will be preserved regardless of the dimensionality of the space. Therefore, in cone-beam reconstruction, contrary to the common assumption, the remarkable locality in 3D Radon inversion formula cannot be used without justification.

Independent of which homogeneous extension we start with, we end up with the $(n-2)th$ differential form of the Radon transform. In order to use the nD Radon inversion formula (Eqn. (2.4)), the $(n-1)th$ differential form needs to be acquired, through the interaction of each cone-beam projection subsystem with the whole Radon space. We call this last differential form the *exterior* differentiation. It will be covered in the next chapter.

3.3.3 Duality

Duality is one of the most important concepts in the Radon transform theorem. We have learned from [Helgason, 1999] that the Radon transform and its inverse can be seen as the analytical counterpart of the geometric *dual* between points and planes in $\mathbb{R}^3$.

In cone-beam reconstruction, however, we have only integrals along lines instead of planes. Lines are self-dual in $\mathbb{R}^3$ [Mundy, 1992], hence there is no direct inversion available. On the other hand, within each cone-beam projection subsystem, a significant dual relation between lines and planes make itself available for us to explore. The line and plane duality in the homogeneous space can be best explained by the following axioms (also see Fig. 3-9):

- Any two distinctive lines determine a plane;

- Any two distinctive planes determine a line.

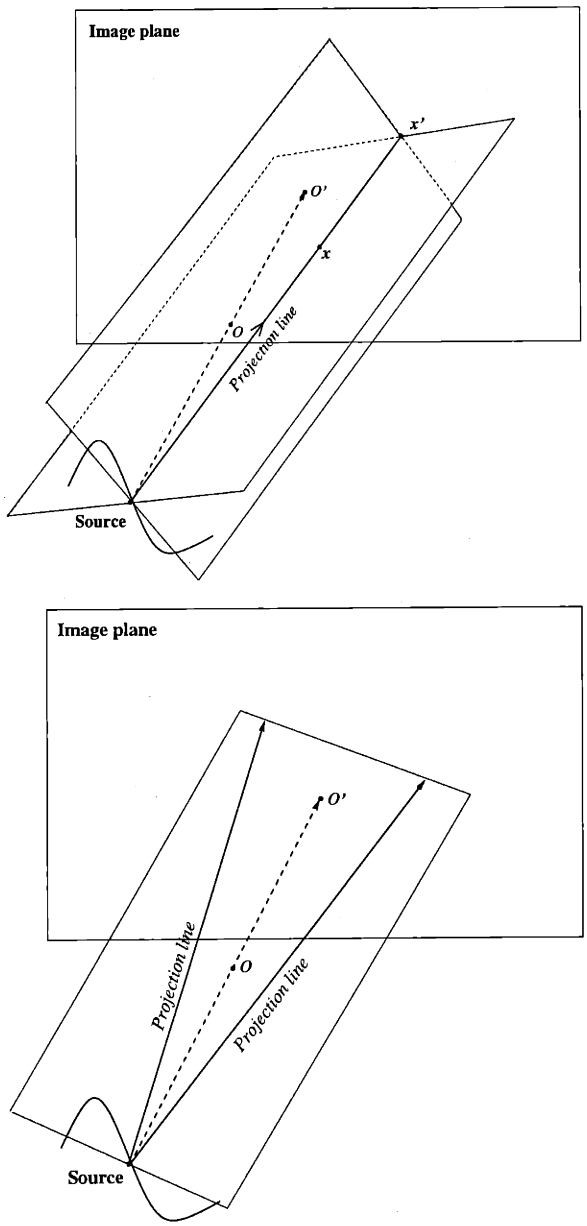

Figure 3-9: *Dual form: lines and planes are dual in the 2D projective subspace*

The complete *dual chain* — from lines to planes back to points, provide us the *key* to invert the straight line projections in cone-beam X-ray tomography.

3.4 Orbital Condition for Exact Reconstruction

The derivation of the **data sufficiency condition** for exact reconstruction in Tuy, Smith and Grangeat is constructive and inherent in their inversion formulae. The key ingredient of this condition is that *all (or almost all) planes passing through the object intersect with the source orbit* — so as to guarantee that points lying in the transform space can be calculated from the available projection measurements.

Our analysis has shown that the validity of this data sufficiency condition has a simple geometric reasoning which is articulated through the *duality principle*, notwithstanding the algebra attached to the homogeneous space during the inverse.

Recall the discussion in the previous section, the lines in $\mathbb{R}^3$ are self-dual, therefore, there is no direct link available to recover the 3D density function from the ray transforms. The inverse reconstruction can only be established, *indirectly*, through the projective space induced by each cone-beam projection. Since now, planes are dually connected to both lines (in the projective space) and points (in $\mathbb{R}^3$). To complete the dual chain, it is necessary that all the planes passing by $\text{supp}(f)$ intersect with the source orbit. It should not be a surprise that *plane* is used as a medium in the statement of the data sufficiency condition. It reveals the dual law governing the geometric relationships in the cone-beam system.

It is clear that a circular orbit (as being used in the Feldkamp algorithm) will not do, since one can construct many planes passing through points that lie above or below the plane of the circle which do not intersect the orbit. Such planes are near parallel to the plane of the circular orbit. The only thing that can be reliably reconstructed from images taken from a circular orbit is the density distribution on the plane of the circle itself.

Chapter 4

The Canonical Cone-beam Inverse

In the homogeneous space induced by each cone-beam projection, H_λ, we have been eluded by an *even* and *odd* puzzle. Now coming out and getting temporarily satisfied with the outcome of the Tuy-Smith-Grangeat relationship, we found ourselves entered the Radon sea and lost *coordinates*.

What Tuy, Smith and Grangeat mainly accomplished so far is the transfer of the cone-beam data into the Radon domain. From an algorithmic point of view, it remains unanswered how the transformed data should be processed in order to recover the original density function. It is easy to discern, in the inversion formulae provided by Tuy, Smith and Grangeat, the differential-backprojection depends on the source curve parameter λ in a very nontrivial way: at each reconstruction site $\boldsymbol{x}$, the integrand in the 3D backprojection need to be evaluated for all planes passing through that point, with normal in all directions $\boldsymbol{\beta} \in \mathbf{S}^2$ and the radial distance determined by $l = \boldsymbol{x} \cdot \boldsymbol{\beta} = \boldsymbol{\Phi}(\lambda) \cdot \boldsymbol{\beta}$. The nontriviality lies in finding the roots for $\boldsymbol{\Phi}(\lambda) \cdot \boldsymbol{\beta} = \boldsymbol{x} \cdot \boldsymbol{\beta}$ (bearing in mind that we are dealing with nonplanar source orbit instead of a planar curve which makes the root finding a nontrivial task). It suggests, at least a sound reason, to let λ initiate the reconstruction so that solving nonlinear equations for each pair of $(\boldsymbol{x}, \boldsymbol{\beta})$ in $(\Omega, \mathbf{S}^2)$ could be eliminated, or reduced in numbers. Another reason to get λ involved more explicitly is that the source curve $\boldsymbol{\Phi}(\lambda)$ characterizes the geometry associated with the cone-beam system and it governs the whole scanning process. So we look into the geometry.

4.1 Cone-beam Geometry

We assume that the 3D source orbit is parameterized by $\mathbf{\Phi}(\lambda) = \big(\phi_1(\lambda),\ \phi_2(\lambda),\ \phi_3(\lambda)\big)$ with λ in a closed interval Λ. We also assume that the following conditions are met:

(1) $\mathbf{\Phi}(\lambda)$ *is outside the convex hull of* $\Omega = \mathrm{supp}(f)$*;*

(2) $\mathbf{\Phi}(\lambda)$ *is an analytic curve which means that its three components* ϕ_1*,* ϕ_2*, and* ϕ_3 *are all analytic functions;*

(3) Almost every plane passing by $\mathrm{supp}(f)$ *intersects with* $\mathbf{\Phi}(\lambda)$ *transversally at least once, that is, for every* $\boldsymbol{x} \in \Omega$ *and almost every* $\boldsymbol{\beta} \in \mathbf{S}^2$*, there exists* $\lambda \in \Lambda$ *such that* $\mathbf{\Phi}(\lambda)\cdot\boldsymbol{\beta} = \boldsymbol{x}\cdot\boldsymbol{\beta}$ *and* $\mathbf{\Phi}'(\lambda)\cdot\boldsymbol{\beta} \neq 0$.

The major difference between our orbital conditions and those of Tuy lies in the *analytic* assumption on $\mathbf{\Phi}(\lambda)$. Most of the simple and nice curves belong to this family.

For convenience of exposition, we will sometimes drop such words like "almost all", "almost every", "almost everywhere" applied to either a set of points on the source orbit, or a set of planes in the Radon space, but bearing in mind that violations are admitted if they constitute only a zero measure set.

4.1.1 Fiber Bundle Structure

In a cone-beam system, we have two independent geometric spaces: one is the vector space spanned by the divergent rays projected from a single point source, the other is the nonplanar orbit on which the X-ray source traverses. These two spaces combined provide information about the Radon space that will become clear later.

The source orbit $\mathbf{\Phi}(\lambda)$ $(\lambda \in \Lambda)$ is a smooth and differentiable 1D manifold, denoted by $\mathbf{B}$. Each point on the source orbit is associated with a 2D projective space of lines passing by that point. This 2D projective space is already known to us from Chapter 3 as the homogeneous space H_λ, indexed by $\lambda \in \Lambda$. Also familiar from Chapter 3, each H_λ, by its line-and-plane duality, can be interchanged with a projective space of planes that has the same projection center. Denote by $\mathbf{P}^2_\lambda$ the projective space of 2D planes. $\mathbf{P}^2_\lambda$ is a 2D

differentiable manifold.

It is clear now that from each point lying on the source orbit grows a projective space consisting of a family of planes. This projective space is a subspace of the Radon space $\mathbf{P}^3$ which includes all the 2D planes in $\mathbb{R}^3$. The density function under reconstruction is compactly supported. Therefore, only those planes intersecting with $\text{supp}(f)$ make contributions during the inverse, since the Radon transform Rf and its derivatives are zero otherwise. It is a sufficient reason to *reduce* the size of the Radon space in our consideration so that it covers only planes through the support of f. We still call this reduced Radon space by the name Radon space assuming no ambiguity could arise in the context of cone-beam reconstruction. Then, if the source orbit conditions are met, the sum $\sum_{\lambda\in\Lambda}\mathbf{P}^2_\lambda$ is a covering space of the Radon space.

The geometric structure described above is called a **fiber bundle** in differential geometry [Kobayashi, 1963], denoted by $\mathbf{T} := \sum_{\lambda\in\Lambda}\mathbf{P}^2_\lambda$ ($\mathbf{T}$ is meant for the total space), with $\mathbf{B}$ and $\mathbf{P}^2$ as its **base space** and **fiber space** respectively. There is a well-defined projection map $\pi : \mathbf{T} \to \mathbf{B}$ on the fiber bundle. For a typical *fiber* we have $\mathbf{P}^2_\lambda := \pi^{-1}(\lambda)$. Each fiber $\mathbf{P}^2_\lambda$ is a submanifold of $\mathbf{P}^3$. The **inclusion map** from $\mathbf{P}^2_\lambda$ to $\mathbf{P}^3$ is given by

$$\tilde{\pi}_\lambda : \beta \longrightarrow (l,\beta)\Big|_{l=\mathbf{\Phi}(\lambda)\cdot\beta}. \tag{4.1}$$

This map is injective, therefore, $\mathbf{P}^2_\lambda$ is embedded in $\mathbf{P}^3$. The embedding map (Eqn. (4.1)) connects the local coordinates (λ,β) of $\mathbf{T}$ to the global coordinates (l,β) of the Radon manifold in a simple manner, that is, $l = \mathbf{\Phi}(\lambda)\cdot\beta$. It suggests that λ may serve as a natural coordinate in both the progressive scanning and reconstruction process.

The fiber bundle $\mathbf{T}$ is also a **trivial fiber bundle** in the sense that its local basis is a Cartesian product of two independent bases from the base space and the fiber space, that is, $\left\{\lambda\in\Lambda\right\}\otimes\left\{\beta\in\mathbf{S}^2\right\}$. This same basis may well be used as a local basis for the Radon space.

Both the base space $\mathbf{B}$ and the fiber space $\mathbf{P}^2$ are differentiable manifolds. Therefore, the fiber bundle $\mathbf{T}$ is differentiable. Locally, the first local coordinate λ relates to the first global

coordinate l by the differentiable map $l = \Phi(\lambda) \cdot \beta$. Hence,

$$\frac{\partial}{\partial l} = \frac{1}{\Phi'(\lambda) \cdot \beta} \frac{\partial}{\partial \lambda}. \tag{4.2}$$

Note that the differential structure of the Radon space is intrinsic and is not affected by the local basis induced by a different selection of the source orbit.

It is worth to mention that the reason why we introduce the fiber bundle is that it characterizes the underlying geometric structure of the cone-beam scanning, and, importantly, it provides a natural mapping, $l = \Phi(\lambda) \cdot \beta$, from the local to the global coordinates of the Radon space. However, the above mapping is not bijective, because some planes in the Radon space are repeated multiple times in $\mathbf{T}$. Denote by $M(\lambda, \beta)$ the number of times that the 2D plane $\boldsymbol{L}_{\Phi(\lambda)\cdot\beta,\beta}$ intersects with the source orbit. Then the same function $M(\lambda, \beta)$, depicts the number of times that the plane $\boldsymbol{L}_{\Phi(\lambda)\cdot\beta,\beta}$ is repeated in $\mathbf{T}$. This $M(\lambda, \beta)$ is called the **redundancy function** or M**-function**,

4.1.2 Dual Space Decomposition

The family of planes passing by a point source constitute only a subset of all the planes in the Radon space. At the end of the scanning process, the covering of the Radon space is completed by $\sum_{\lambda \in \Lambda} \mathbf{P}_\lambda^2$. In this sense we say that the Radon space, the so-called dual space, can be *decomposed*. To be able to describe the geometric constraint raised by each cone-beam projection, we pick up a point source, say S, and a **projection line** that connects the source S to a point P on the image plane. Then for each point Q lying on SP, the family of planes passing by both S and Q intersect at SP. As a result, the normal directions of this set of planes are perpendicular to the projection line SP and are confined to a great circle on the backprojection sphere surrounding Q (see Fig. 4-1). We name the great circle the **backprojection circle**.

It is easy to see that the effect of rotating the X-ray source around the test object is to provide many different backprojection orientations so that the 3D backprojection sphere can be fully covered (see Fig. 4-2).

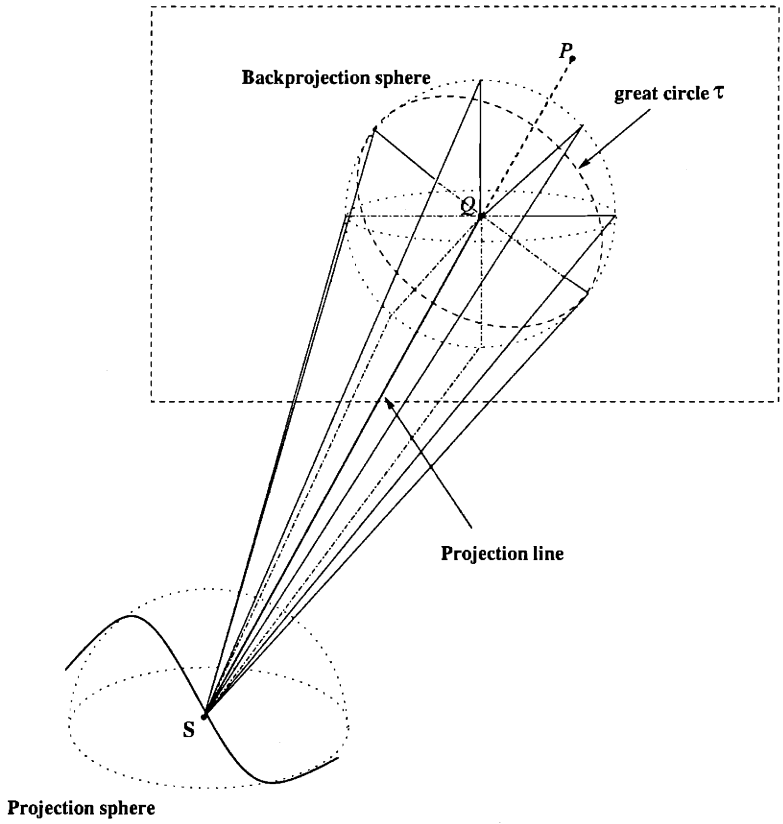

Figure 4-1: *A bundle of Radon planes interesting at a projection line*

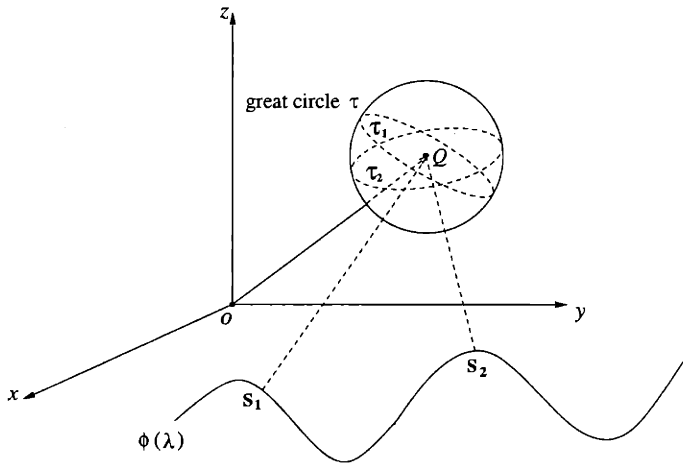

Figure 4-2: *Backprojection orientations vary from projection to projection*

Note that the rotational pattern of the 2D great circles on the backprojection sphere is different from point to point in the object space. A remaining question is how this rotation shall be analytically formulated. A related problem in the object space, which is an Euclidean space, is how to set up local frames so that the sequential cone-beam projections under the unique movement of the X-ray source can be locally described. These local frames shall be convenient for transformation between projections, and convenient to transform from local coordinates to their commonly shared global coordinates.

As one can see in our earlier discussion, the basis $\Big\{\lambda \in \Lambda\Big\} \times \Big\{\beta \in \mathbf{S}^2\Big\}$ is naturally formed in the transform space, the Radon space of 2D planes, not in the object space. It is not suitable for our current request.

We consult the famous **method of moving frames** [Carmo, 1976], with its earliest appearance found in Fresnel's treatment of space curves, and later substantially developed and generalized by Cartan. In the case of a continuous and differentiable source orbit, we can make use of the normalized principal direction, denoted by $\boldsymbol{\gamma}(\lambda) = \boldsymbol{\Phi}(\lambda)/|\boldsymbol{\Phi}(\lambda)|$, and construct an orthogonal local frame consisting of the following basis:

$$\boldsymbol{R}(\lambda) = \big(\boldsymbol{\gamma}'(\lambda),\ \boldsymbol{\gamma}(\lambda),\ \boldsymbol{\gamma}'(\lambda) \times \boldsymbol{\gamma}(\lambda)\big). \tag{4.3}$$

It generates a set of 3-by-3 orthogonal matrices as λ ranges in the indexing set Λ. These matrices are associated to a set of consecutive rotations. By this construction, the sequential X-ray projections induce a rotational group transformation on both $\mathbb{R}^3$ and the projective subspace $\mathbf{P}^2$ attached to the source orbit.

The potential leverage of the moving frame method in cone-beam reconstruction has not been fully understood and explored so far. In fact, the importance of the moving frame representation in cone-beam reconstruction is no small amount. Other than its convenience in transferring two consecutive image coordinates, it is also responsible for transformation of the projective basis in the Radon space. Amazingly, the same rotational group transformation simultaneously describes the coordinate transform in both object space and the transform space. To explain this, we notice that in the transform space, the family of planes passing by each point Q and an X-ray source S are represented by a unit circle on

the backprojection sphere surrounding Q. This circle is perpendicular to the source-to-point line SQ. When the X-ray source is moved around the object, it seems to rotate around Q and the unit circle therefore changes its orientation while still remaining on the backprojection sphere. This is a rigid motion. And Carton's orthogonal moving frames provide us a machinery to describe such a motion.

So now, we have acquired an intuitive understanding of the cone-beam geometry, in both its imaging space and the transform space. In the transform space, we have found that the internal structure of the 3D backprojection has a simpler *decomposed* form which can be described by a set of orthogonal transformations of a 2D backprojection. The transformations are formulated by the 3-by-3 orthogonal matrices (Eqn. (4.3)) which are well known as Cartan's moving frames, with the local origin anchored on the source orbit.

In the next section, we will derive from the 3D Radon inverse a new inversion formula to accommodate the cone-beam projective geometry. It will achieve the geometric decomposition described here in an analytical form.

4.2 The Canonical Cone-beam Inversion Formula

Before we can switch coordinates from l to λ and derive our new inversion formula, we make a short detour to address the issue of non-bijective nature of the mapping $l = \mathbf{\Phi}(\lambda) \cdot \boldsymbol{\beta}$.

4.2.1 Analytic Curves

Given an analytic curve, all its components are analytic functions. An analytic function has the following nice properties:

A. It can be locally described by a power series.

B. The analytic function is constant if it has a constantly-valued segment.

C. A analytic function consists of isolated and finite number of critical points on a closed interval unless it is constant.

Note that only constantly-valued functions have infinite number of critical points.

Under our assumption that the source orbit $\mathbf{\Phi}(\lambda)$ is analytic and non-planar (implicit in condition (3)), we have:

Lemma 4.1 *For every $\boldsymbol{\beta} \in \mathbf{S}^2$, there exists a finite number of disconnected intervals so that the inverse mapping of $l = \mathbf{\Phi}(\lambda) \cdot \boldsymbol{\beta}$ is injective on each of these interval.*

Proof: Let's choose an arbitrary $\boldsymbol{\beta}$. Denote by $\boldsymbol{L}_{0,\boldsymbol{\beta}}$ the plane that has normal $\boldsymbol{\beta}$ and goes through the origin. Denote by $\boldsymbol{L}_{\mathbf{\Phi}(\lambda)\cdot\boldsymbol{\beta},\boldsymbol{\beta}}$ the plane with normal $\boldsymbol{\beta}$ and passing by $\mathbf{\Phi}(\lambda)$. The plane $\boldsymbol{L}_{0,\boldsymbol{\beta}}$ shall be called the **level plane**. Then, the dot product $l = \mathbf{\Phi}(\lambda) \cdot \boldsymbol{\beta}$ can be interpreted as the elevated height of the plane $\boldsymbol{L}_{\mathbf{\Phi}(\lambda)\cdot\boldsymbol{\beta},\boldsymbol{\beta}}$ above or below the level plane (see Fig. 4-3).

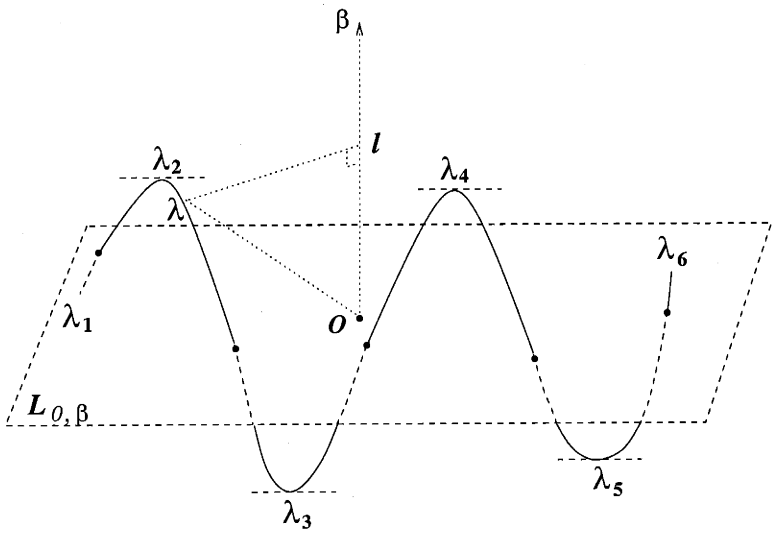

Figure 4-3: *A space curve and its relationship with 2D planes*

The orbit $\mathbf{\Phi}(\lambda)$ is an analytic curve, therefore $l(\lambda) = \mathbf{\Phi}(\lambda) \cdot \boldsymbol{\beta}$ is an analytic function. Moreover, $\mathbf{\Phi}(\lambda)$ is nonplanar, it is easy to verify that $l(\lambda) \neq$ constant. By the property (C) of the analytic function, $l(\lambda)$ has only a finite number of critical points that satisfy $l'(\lambda) = \mathbf{\Phi}'(\lambda) \cdot \boldsymbol{\beta} = 0$. Denote by $\lambda_1, \lambda_2, \cdots, \lambda_{m(\boldsymbol{\beta})}$ the complete set of the critical points for $l(\lambda) = \mathbf{\Phi}(\lambda) \cdot \boldsymbol{\beta}$. This allows us to construct the following disjoint intervals:

$$\Lambda_i = [\lambda_i, \lambda_{i+1}] \quad \text{for } i = 1, 2, \cdots, m(\boldsymbol{\beta}) - 1. \tag{4.4}$$

Now, suppose that the inverse mapping of $l(\lambda) = \mathbf{\Phi}(\lambda) \cdot \boldsymbol{\beta}$ is not injective on one such interval, say Λ_i, which means that there are a dual or multiple images of certain l on Λ_i. It implies that $l = \mathbf{\Phi}(\lambda) \cdot \boldsymbol{\beta}$ has at least two distinctive roots on the interval Λ_i. Denote by $\lambda_i^{(1)}$ and $\lambda_i^{(2)}$ the two distinctive roots, then $\lambda_i \leq \lambda_i^{(1)} \leq \lambda_i^{(2)} \leq \lambda_{i+1}$. By the *mean-value theorem* and the property (B), (C) of the analytic function, we can find at least one critical point strictly between $\lambda_i^{(1)}$ and $\lambda_i^{(2)}$ such that $l'(\lambda) = \mathbf{\Phi}'(\lambda) \cdot \boldsymbol{\beta} = 0$, contradict to the previous assumption that $\lambda_1, \lambda_2, \cdots, \lambda_{m(\boldsymbol{\beta})}$ are the only roots for $l'(\lambda) = \mathbf{\Phi}'(\lambda) \cdot \boldsymbol{\beta} = 0$. It settles our proof. ■

For each $\boldsymbol{\beta} \in \mathbf{S}^2$, a plane perpendicular to $\boldsymbol{\beta}$ can only intersect with the source orbit finite number of times, since each interval constructed in our proof of Lemma 4.1 allows no more than one of such intersections, and the number of intersections is bounded by the number of intervals. We conclude then

Lemma 4.2 *For every $\boldsymbol{\beta} \in \mathbf{S}^2$, the redundancy function $M(\lambda, \boldsymbol{\beta})$ is bounded.*

4.2.2 Inversion Formula

Equipped with an intuitive understanding of the cone-beam geometry and the nature of the mapping $l = \mathbf{\Phi}(\lambda) \cdot \boldsymbol{\beta}$, we now start with the 3D Radon inversion formula Eqn. (2.10):

$$f(\boldsymbol{x}) = -\frac{1}{8\pi^2} \int_{\mathbf{S}^2} \left. \frac{\partial^2 Rf(l, \boldsymbol{\beta})}{\partial l^2} \right|_{l=\boldsymbol{x}\cdot\boldsymbol{\beta}} d\boldsymbol{\beta}.$$

Our goal is to express the backprojection operator in the above formula in terms of the natural coordinate λ. We also expect that such a change of variables will results in a *decomposed form* of the 3D backprojection operator since each cone-beam projection gives rise to a geometric constraint which confines the backprojection orientations onto a set of great circles.

Theorem 4.1 *With cone-beam geometry, 3D Radon inversion formula Eqn. (2.10) can be*

reformulated explicitly in terms of the source orbit parameter λ by

$$f(\boldsymbol{x}) = -\frac{1}{8\pi^2}\int_{\Lambda}\left\{\int_{\boldsymbol{\beta}\in\left\{\boldsymbol{x}-\boldsymbol{\Phi}(\lambda)\right\}^{\perp},\ \boldsymbol{\beta}\in\mathbf{S}^2} R''f(\boldsymbol{\Phi}(\lambda)\cdot\boldsymbol{\beta},\boldsymbol{\beta})\frac{|\boldsymbol{\Phi}'(\lambda)\cdot\boldsymbol{\beta}|}{M(\lambda,\boldsymbol{\beta})}\,d\boldsymbol{\beta}\right\}\,d\lambda, \tag{4.5}$$

where $\left\{\boldsymbol{x}-\boldsymbol{\Phi}(\lambda)\right\}^{\perp}$ denotes the plane perpendicular to $\boldsymbol{x}-\boldsymbol{\Phi}(\lambda)$ and through the origin. The derivative in $R''f$ acts on its first variable, and $M(\lambda,\boldsymbol{\beta})$ is the redundancy function.

Note that the inner integral in the above equation is a 2D backprojection over the unit circle perpendicular to the projection ray $\boldsymbol{x}-\boldsymbol{\Phi}(\lambda)$, and each plane $\boldsymbol{L}_{\boldsymbol{\Phi}(\lambda)\cdot\boldsymbol{\beta},\boldsymbol{\beta}}$ is weighted by its multiplicity in the fiber bundle space $\mathbf{T}$.

Proof: In Eqn. (2.10), the backprojection integrand, $R''f$, is evaluated at $l=\boldsymbol{x}\cdot\boldsymbol{\beta}$. In terms of the *dirac delta* function, Eqn. (2.10) can be expressed as

$$\begin{aligned} f(\boldsymbol{x}) &= -\frac{1}{8\pi^2}\int_{\mathbf{S}^2}\int_{-\infty}^{\infty} R''f(l,\boldsymbol{\beta})\delta(l-\boldsymbol{x}\cdot\boldsymbol{\beta})\,dl\ \ d\boldsymbol{\beta} \\ &= -\frac{1}{8\pi^2}\int_{\mathbf{S}^2}\int_{-L}^{L} R''f(l,\boldsymbol{\beta})\delta(l-\boldsymbol{x}\cdot\boldsymbol{\beta})\,dl\ \ d\boldsymbol{\beta} \end{aligned} \tag{4.6}$$

for some finite bound L. The last identity holds because the density function in our study is compactly supported. Therefore, Rf and its derivatives are finitely supported.

For a fixed $\boldsymbol{\beta}$, by Lemma 4.1, we can find a finite number of intervals, denoted by Λ_i ($i=1,2,\cdots,m(\boldsymbol{\beta})-1$), such that on each Λ_i the inverse mapping of $l=\boldsymbol{\Phi}(\lambda)\cdot\boldsymbol{\beta}$ is injective. When switching from the global coordinates $(l,\boldsymbol{\beta})$ to the local coordinates $(\lambda,\boldsymbol{\beta})$, separately on each interval Λ_i ($i=1,2,\cdots,m(\boldsymbol{\beta})-1$), the inner integrand of Eqn. (4.6) boils down to

$$\int_{\Lambda_i} R''f(\boldsymbol{\Phi}(\lambda)\cdot\boldsymbol{\beta},\boldsymbol{\beta})\delta(\boldsymbol{\Phi}(\lambda)\cdot\boldsymbol{\beta}-\boldsymbol{x}\cdot\boldsymbol{\beta})|\boldsymbol{\Phi}'(\lambda)\cdot\boldsymbol{\beta}|\,d\lambda. \tag{4.7}$$

The above equation shall be interpreted by

$$R''f(\boldsymbol{\Phi}(\lambda)\cdot\boldsymbol{\beta},\boldsymbol{\beta}) = \begin{cases} R''f(\boldsymbol{\Phi}(\lambda)\cdot\boldsymbol{\beta},\boldsymbol{\beta}), & \text{for } \lambda\in\Lambda_i \\ 0, & \text{otherwise} \end{cases}. \tag{4.8}$$

Hence, Eqn. (4.7) is nonzero if and only if there exists a root for $\boldsymbol{\Phi}(\lambda)\cdot\boldsymbol{\beta}=\boldsymbol{x}\cdot\boldsymbol{\beta}$ on the interval Λ_i.

Then the summation over the index i yields

$$\int_{\Lambda} R''f(\boldsymbol{\Phi}(\lambda)\cdot\boldsymbol{\beta},\boldsymbol{\beta})\delta(\boldsymbol{\Phi}(\lambda)\cdot\boldsymbol{\beta}-\boldsymbol{x}\cdot\boldsymbol{\beta})|\boldsymbol{\Phi}'(\lambda)\cdot\boldsymbol{\beta}|\,d\lambda. \tag{4.9}$$

However, this sum is different from $\int_{-L}^{L} R''f(l,\boldsymbol{\beta})\delta(l-\boldsymbol{x}\cdot\boldsymbol{\beta})\,dl$, because each plane $\boldsymbol{L}_{\boldsymbol{\Phi}(\lambda)\cdot\boldsymbol{\beta},\boldsymbol{\beta}}$ is subject to multiple covering in the fiber bundle space. The repetition is finite (by Lemma 4.2) therefore summable. A simple remedy is to divide by the M-function $M(\lambda,\boldsymbol{\beta})$ to eliminate the redundancy in the calculation when we switch from l to λ. The result is

$$f(\boldsymbol{x})=-\frac{1}{8\pi^2}\int_{\mathbf{S}^2}\int_{\Lambda} R''f(\boldsymbol{\Phi}(\lambda)\cdot\boldsymbol{\beta},\boldsymbol{\beta})\delta(\boldsymbol{\Phi}(\lambda)\cdot\boldsymbol{\beta}-\boldsymbol{x}\cdot\boldsymbol{\beta})\frac{|\boldsymbol{\Phi}'(\lambda)\cdot\boldsymbol{\beta}|}{M(\lambda,\boldsymbol{\beta})}\,d\lambda\;\,d\boldsymbol{\beta}. \tag{4.10}$$

Note that if $M(\lambda,\boldsymbol{\beta})=0$, $R''f(\boldsymbol{\Phi}(\lambda)\cdot\boldsymbol{\beta},\boldsymbol{\beta})$ actually does not contribute to the integral, therefore the appearance of singularity in the denominator is false. We can simply reassign the value of the M-function by $M(\lambda,\boldsymbol{\beta})=+\infty$ for those $M(\lambda,\boldsymbol{\beta})=0$.

Then, by changing the order of the integration in Eqn. (4.10), we get

$$f(\boldsymbol{x})=-\frac{1}{8\pi^2}\int_{\Lambda}\left\{\int_{\mathbf{S}^2} R''f(\boldsymbol{\Phi}(\lambda)\cdot\boldsymbol{\beta},\boldsymbol{\beta})\delta((\boldsymbol{\Phi}(\lambda)-\boldsymbol{x})\cdot\boldsymbol{\beta})\frac{|\boldsymbol{\Phi}'(\lambda)\cdot\boldsymbol{\beta}|}{M(\lambda,\boldsymbol{\beta})}\,d\boldsymbol{\beta}\right\}\,d\lambda. \tag{4.11}$$

The *dirac delta* function selects only $\boldsymbol{\beta}$ in the directions perpendicular to $\boldsymbol{\Phi}(\lambda)-\boldsymbol{x}$, hence

$$f(\boldsymbol{x})=-\frac{1}{8\pi^2}\int_{\Lambda}\left\{\int_{\boldsymbol{\beta}\in\left\{\boldsymbol{x}-\boldsymbol{\Phi}(\lambda)\right\}^{\perp},\boldsymbol{\beta}\in\mathbf{S}^2} R''f(\boldsymbol{\Phi}(\lambda)\cdot\boldsymbol{\beta},\boldsymbol{\beta})\frac{|\boldsymbol{\Phi}'(\lambda)\cdot\boldsymbol{\beta}|}{M(\lambda,\boldsymbol{\beta})}\,d\boldsymbol{\beta}\right\}\,d\lambda. \tag{4.12}$$

This completes our proof. ∎

We notice that the *dirac delta* function is our main trick in deriving the new inversion formula. It is appropriate to use in the context of our derivation because of the summability over the finite number of intervals Λ_i (Lemma 4.1) and the boundedness of the number of the plane-orbit intersections (Lemma 4.2).

Reading from Eqn. (4.5), there is, at each fixed source position, only one 2D backprojection need to be performed along each projection ray. The resulting value is constantly assigned to all the points lying on that ray. The ambiguity naturally occurring within one single cone-beam projection is due to the fact that points on the same ray are in the same equivalent class. This uncertainty shall be resolved when information from projections of all directions are combined.

Our inversion formula reveals the geometric structure of the 3D backprojection operator. It differs fundamentally from all previous inversion formulae by reducing the backprojection from 3D to 2D with explicit dependency on the source orbit. This makes the reconstruction more direct and can be easily described. Even though without this formula, we can still obtain cone-beam reconstruction algorithm based on the analysis conducted in section 4.1 alone, it is obvious that Eqn. (4.5) gives a compact geometric description of the backprojection, from which we can almost visualize the solution procedure.

Since the source orbit is sampled, the outer integral of Eqn. (4.5) should be numerically treated as a Riemann sum:

$$f(\boldsymbol{x}) = -\frac{1}{8\pi^2}\sum_i \left\{ \int_{\boldsymbol{\beta}\in\left\{\boldsymbol{x}-\boldsymbol{\Phi}(\lambda_i)\right\}^{\perp},\boldsymbol{\beta}\in\mathbf{S}^2} R''f(\boldsymbol{\Phi}(\lambda_i)\cdot\boldsymbol{\beta},\boldsymbol{\beta})\frac{|\boldsymbol{\Phi}'(\lambda_i)\cdot\boldsymbol{\beta}|}{M(\lambda_i,\boldsymbol{\beta})}\,d\boldsymbol{\beta} \right\}(\lambda_{i+1}-\lambda_i). \quad (4.13)$$

The inner integral can be discretized by:

$$\sum_{j=0}^{N-1} R''f(\boldsymbol{\Phi}(\lambda_i)\cdot\boldsymbol{\beta}_j,\boldsymbol{\beta}_j)\frac{|\boldsymbol{\Phi}'(\lambda_i)\cdot\boldsymbol{\beta}_j|}{M(\lambda_i,\boldsymbol{\beta}_j)}\Delta\theta \quad (4.14)$$

where $\boldsymbol{\beta}_j = \cos\theta_j\boldsymbol{\alpha}^{\perp_1} + \sin\theta_j\boldsymbol{\alpha}^{\perp_2}$, $\theta_j = (2\pi j)/N$ $(j = 0, 1, \cdots, N-1)$ and $\Delta\theta = \dfrac{2\pi}{N}$ is the discretization step. The unit vectors $\boldsymbol{\alpha} = \boldsymbol{x} - \boldsymbol{\Phi}(\lambda_i)/|\boldsymbol{x} - \boldsymbol{\Phi}(\lambda_i)|$, $\boldsymbol{\alpha}^{\perp_1}$ and $\boldsymbol{\alpha}^{\perp_2}$ form an orthonormal basis.

Eqn. (4.5) produces the well-known summation-filtered-backprojection formula. It allows progressive refinement during the image reconstruction. Note that M-function determines the contribution of each measurement. It shall be precalculated for a selected source orbit.

4.3 The Exterior Differentiation

In the preceding sections, we have focused largely on the backprojection operator and we have derived a decomposed formula of the 3D Radon inverse. However, the link between the cone-beam data and the $2nd$-order derivative of the Radon transform is yet to be established in terms of the natural coordinate λ.

Tuy, Smith and Grangeat's work enables the transfer of the cone-beam data to some intermediate functions related to the first radial derivative of the Radon transform. Since each cone-beam projection does not provide parallel planes, it is obvious that an exterior differentiation or filtering is needed so that the intermediate functions can be transformed to the second radial derivative $R''f$.

Now we look at the differential structure of the fiber bundle $\mathbf{T}$. It is a covering space of the Radon space, and is locally differentiable. Since the local basis for $\mathbf{T}$ is also a local basis for $\mathbf{P}^3$, the Radon space, differentiation with respect to the global coordinate l can therefore be assessed by differentiation with respect to the local coordinate λ. Another way to see this is to imagine a set of parallel planes in a near neighborhood, the infinitesimal changes in l can be viewed as infinitesimal changes in λ (see Fig. 4-4). In turn, if we take an infinitesimal step along the tangent direction of the source orbit, we will certainly find a plane parallel to the one we started with. It is natural therefore to differentiate over the parallel plane with respect to parameter λ of the source orbit.

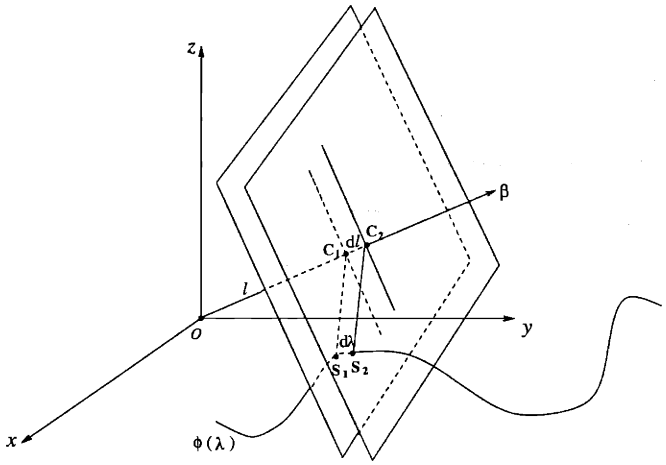

Figure 4-4: *Differentiating over parallel planes.*

We start with Grangeat's intermediate function $R'f$, switching the coordinates from l to λ by the inverse of the differentiable map $l = \mathbf{\Phi}(\lambda) \cdot \boldsymbol{\beta}$ yields

$$R''f(\mathbf{\Phi}(\lambda) \cdot \boldsymbol{\beta}, \boldsymbol{\beta}) = \frac{1}{\mathbf{\Phi}'(\lambda) \cdot \boldsymbol{\beta}} \frac{\partial R'f(\mathbf{\Phi}(\lambda) \cdot \boldsymbol{\beta}, \boldsymbol{\beta})}{\partial \lambda}, \tag{4.15}$$

where $R''f$ is read as the $2nd$-order partial derivative of the Radon transform with respect to the radial parameter l at $l = \mathbf{\Phi}(\lambda) \cdot \boldsymbol{\beta}$. Note that $R'f(\mathbf{\Phi}(\lambda) \cdot \boldsymbol{\beta}, \boldsymbol{\beta})$, obtained from a cone-beam image, is now considered as a "function" of λ, which is a natural result of the progressive scanning process. The differentiation over continuous images was unfamiliar to us earlier, but it should not be such a surprise if we compare it to the differentiation over parallel planes. Their spirit are the same.

The discrete version of Eqn. (4.15) is

$$R''f(\mathbf{\Phi}(\lambda_i) \cdot \boldsymbol{\beta}, \boldsymbol{\beta}) = \frac{1}{\mathbf{\Phi}'(\lambda_i) \cdot \boldsymbol{\beta}} \frac{R'f(\mathbf{\Phi}(\lambda_{i+1}) \cdot \boldsymbol{\beta}, \boldsymbol{\beta}) - R'f(\mathbf{\Phi}(\lambda_i)) \cdot \boldsymbol{\beta}, \boldsymbol{\beta})}{\lambda_{i+1} - \lambda_i}. \tag{4.16}$$

It is the first order approximation through a one-step finite difference. Higher order approximation can be achieved by engaging more cone-beam images. It means that a few more images shall be acquired in advance.

Tuy's inversion formula (Eqn. (3.5)) captures the concept of the exterior differentiation. That is also the reason why Tuy's source orbit condition is the most accurate among the three. It imposes a transversality condition on the plane and orbit intersections which we will analyze soon.

From the discussion in Section 3.3, Tuy's intermediate function G_1 can be split into even and odd parts. The odd part (which is also the imaginary part) of G_1 corresponds to the first radial derivative of the Radon transform, $R'f$. The even part (also the real part) of G_1 corresponds to the Hilbert transform of $R'f$ which is Smith's intermediate function G_2:

$$G_1(\lambda, \boldsymbol{\beta}) = \frac{1}{2} G_2(\lambda, \boldsymbol{\beta}) + \frac{1}{4\pi i} R'f(\lambda, \boldsymbol{\beta}). \tag{4.17}$$

Then taking the exterior differentiation with respect to λ, we have

$$\frac{1}{2\pi i\boldsymbol{\Phi}(\lambda)\cdot\boldsymbol{\beta}}\frac{\partial G_1(\lambda,\boldsymbol{\beta})}{\partial\lambda}=\frac{1}{4\pi i\boldsymbol{\Phi}'(\lambda)\cdot\boldsymbol{\beta}}\frac{\partial G_2(\lambda,\boldsymbol{\beta})}{\partial\lambda}-\frac{1}{8\pi^2}R''f(\lambda,\boldsymbol{\beta}). \tag{4.18}$$

Now the real part becomes $R''f$ which is even, the imaginary part becomes odd and it will not survive the backprojection. It turns out that Tuy's inversion formula eventually boils down to the 3D Radon inverse (Eqn. (2.10)).

Smith's intermediate function requires a ramp-filtering over all the parallel planes in the Radon space, which can be expressed by

$$R''f(\boldsymbol{\Phi}(\lambda)\cdot\boldsymbol{\beta},\boldsymbol{\beta})=\mathcal{H}_l\Big\{G_2(\boldsymbol{\Phi}(\lambda)\cdot\boldsymbol{\beta},\boldsymbol{\beta})\Big\}\Big|_{l=\boldsymbol{\Phi}(\lambda)\cdot\boldsymbol{\beta}}. \tag{4.19}$$

The computation of the global filtering is too costly and is not efficient compared to the local operations in the previous two cases.

What happens when $\boldsymbol{\Phi}'(\lambda)\cdot\boldsymbol{\beta}=0$?

The exceptional case $\boldsymbol{\Phi}'(\lambda)\cdot\boldsymbol{\beta}=0$ corresponds to the situation where the Radon plane $\boldsymbol{L}_{\boldsymbol{\Phi}(\lambda)\cdot\boldsymbol{\beta},\boldsymbol{\beta}}$ meets with the source orbit tangentially. When the X-ray source moves along the tangential direction of its orbit, there are certain planes that stay still and do not move. These planes have normal directions perpendicular to the tangent $\boldsymbol{\Phi}'(\lambda)$. Under such circumstances, the radial derivative can not be calculated. It happens on a set of planes within every cone-beam projection. The reason that they are admitted in a strictly mathematical term is because the family of planes which have normal direction perpendicular to $\boldsymbol{\Phi}'(\lambda)$ constitute only a zero measure set. However, this suggests that there are sensitivity issues that need to be further investigated. Since the measurements are not noise-free and data interpolation also produces error, the discrepancy in the transformed data from consecutive cone-beam projections on those planes that are not moving will be magnified by $\Delta\lambda$. For this reason, we want to avoid those problematic points, and hope, that almost every plane passing by supp(f) intersects with the source orbit transversally at least once, so that the Radon derivative not only can be evaluated, but can be done in a stable manner as well. This is the stability condition addressed by Finch [Finch, 1985].

4.4 Reconstruction Algorithms

The previous discussion prepares us to obtain, in general, an inverse procedure for cone-beam reconstruction which can be described as follows:

Cone-beam reconstruction is iteration over:

Step 1: At a source location λ, obtain from the cone-beam image the transform function $G_1(\lambda,\beta)$, or $G_2(\lambda,\beta)$ or $R'f(\lambda,\beta)$.

Step 2: Perform an exterior filtering across the projections, that is, filtering over images of G_1, G_2 and $R'f$ obtained from consecutive cone-beam projections. This step yields the second radial derivative of the Radon transform:

$$R''f(\Phi(\lambda)\cdot\beta,\beta) = \frac{1}{2\pi\Phi'(\lambda)\cdot\beta}\frac{\partial\,\mathrm{Im}\{G_1(\lambda,\beta)\}}{\partial\lambda}, \tag{4.20}$$

$$R''f(\Phi(\lambda)\cdot\beta,\beta) = \mathcal{H}_l\Big\{G_2(\Phi(\lambda)\cdot\beta,\beta)\Big\}\Big|_{l=\Phi(\lambda)\cdot\beta}, \tag{4.21}$$

$$R''f(\Phi(\lambda)\cdot\beta,\beta) = \frac{1}{\Phi'(\lambda)\cdot\beta}\frac{\partial R'f(\lambda,\beta)}{\partial\lambda}. \tag{4.22}$$

Step 3: Back project the second radial derivative of the Radon transform on a 2D unit circle perpendicular to each projection line to generate a 3D partial image with constant values assigned along each projection ray. This step shall be implemented in a parallel fashion for all the rays emitted from one single point source.

Step 4: The resulting 3D partial image from Step 3 is superposed to the previous intermediate result.

Step 5: Move the X-ray source and go back to Step 1 till the scanning process ends.

Theoretical work done by Tuy, Smith and Grangeat each serves as a good starting point – their initial treatment of each cone-beam image leads to an intermediate function in the Radon space. These results shall be viewed as intermediate-staged reconstruction. It takes

a few more steps to complete the final reconstruction:

- *Differentiate or perform filtering between the projections;*
- *Back project the result along each projection ray to produce a 3D image as a partial reconstruction;*
- *Sum over all the partial results.*

The inverse procedure has two distinctive recipes according to where we start. If we begin with Tuy or Grangeat's intermediate function, reconstruction is in the form of *summation-differentiation-backprojection* — only a few images are required to be collected ahead of time for a partial reconstruction. Whereas, reconstruction based on Smith's intermediate function is not local and is characterized by *summation-convolutional-backprojection* — where ramp filtering is performed over the parallel Radon planes passing through the scanned object. Since differentiation and convolution are both considered to be a *filtering* process, we make no distinction of them by using *summation-filtered-backprojection* for the purpose of a unifying treatment. But it is clear that Tuy and Grangeat's intermediate function requires only local filtering whereas Smith's intermediate function requires global filtering.

This inverse procedure carries a significant geometric structure that can be described through the following diagram:

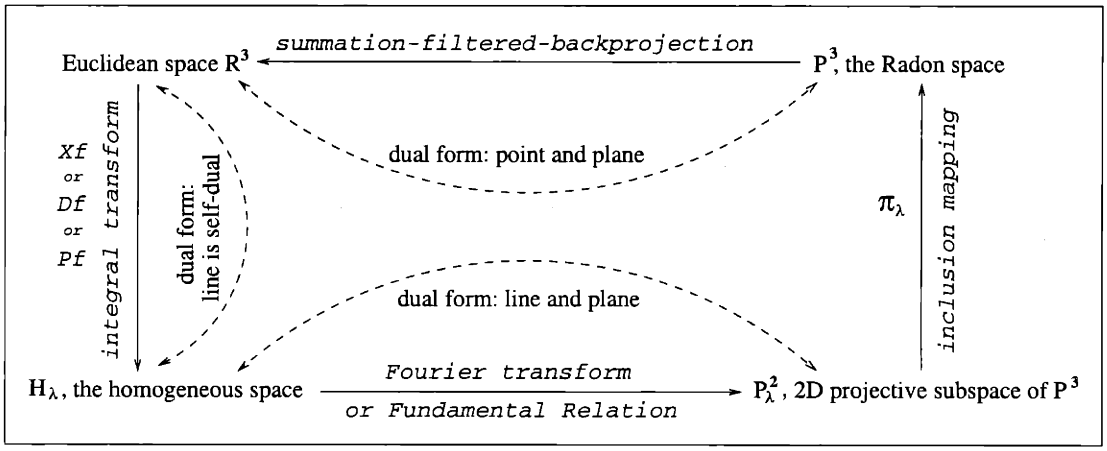

Figure 4-5: *Cone-beam reconstruction: forward and inverse procedures, the related geometric spaces and their dual forms.*

In this process, geometry and algebra cohabit in a lively form. Thay are hand in hand, however, each renders a separate, interesting thread (see Fig. 4-5).

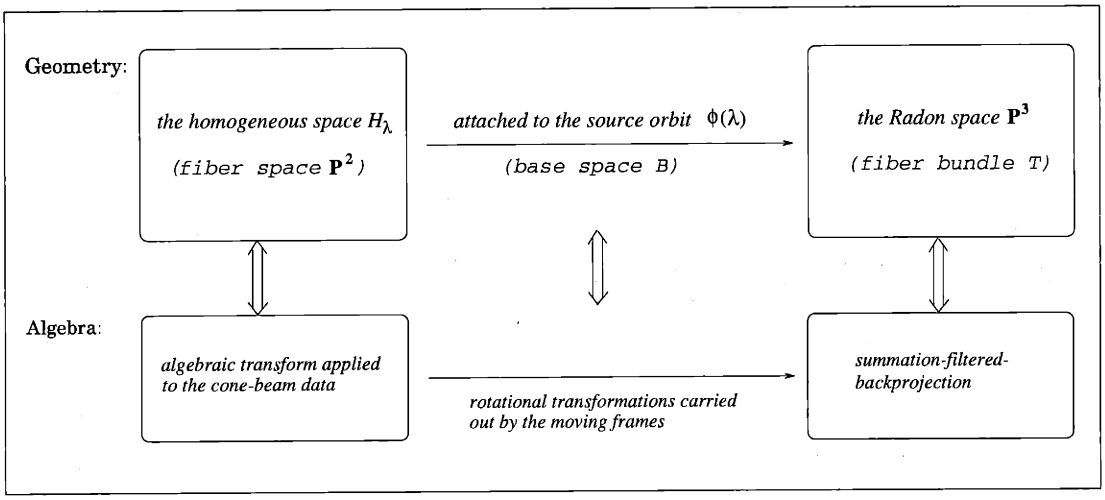

Figure 4-6: *Cohabited geometry and algebra in cone-beam reconstruction.*

Geometry possesses the perceptual power and algebra is the impetus for the vital computational dynamics. Through Radon, we can almost *see* the solution through our imaginative eye. What a grace! As elegant as Radon, Cartan's moving frames provide us a vehicle to travel along the source orbit and accomplish the computational task in a clean form.

With the new inversion formula, the complexity of the reconstruction algorithms is reduced. Assume n is the edge size of the volume. Also assume that we have chosen a finite number of source positions as well as a finite number of normal directions β distributed on the unit sphere. Then for each cone-beam image, we have n^2 projection rays to process. If we use Grangeat's intermediate function, then along each projection ray, a set of $1st$-order radial derivative need to be obtained which takes $O(n)$ time. The resulting algorithm has complexity $O(mn^3)$ where m depends on the number of source positions as well as the number of orientations β used in the 2D backprojection.

4.5 A General Discussion

The idea presented in this chapter can be easily generalized as long as the feature of fiber bundle remains as the overall structure. The benefit of using the fiber bundle structure is

that the base space and the fiber space are relatively independent entities. It allows diversity in the fiber bundle compositions by thinking of various fiber spaces while confining the X-ray source on a 1D manifold. It keeps the overall reconstruction procedure unchanged. For example, the 1D projective fiber space leads us to the fan-beam geometry, $(n-1)D$ projective fiber space leads to something that may go by the name nD cone-beam, and $(n-1)$D subspace of parallel rays carries us to the parallel-beam geometry. All these different scanning modalities are variations of the same geometric principle. With slight modification, our inverse procedure can be applied, the backprojection can still be decomposed in a similar fashion and lend itself an efficient implementation.

So far, the inverse procedure is characterized significantly in terms of geometry. It has potential to be used in a more general context of inverse reconstructions related to the Radon transform. We notice here that the diversity is a remarkable strength of the Radon transform which makes it all possible for vast generalizations.

Chapter 5

Choice of Source Orbit on Sampling Performance

The arrangement of the X-ray source and the detector plane contributes to the sampling density distribution in the transform space. In this chapter, we present a theoretical analysis of the sampling condition related to the source orbit.

Good design of the source orbit not only improves the accuracy of the reconstruction but also helps to reduce the patient's exposure to radiation because lower X-ray exposure is needed to reach a desired image quality. So far, little attention has been paid to this important problem.

We consider two cases: (i) the parallel-beam projection (distant source) where the "working space" is the Fourier spectrum space, and (ii) the true cone-beam projection (nearby source), where the "working space" is the Radon space. It is instructive to consider the parallel-beam projection because the mathematics is simpler and because it provides immediate insight. The parallel-beam projection is a limiting case (as the source is put at a distance) of the cone-beam projection. It in turn helps to facilitate and test our fundamental understanding of the sampling in the cone-beam case. A sinusoidal orbit will be used to illustrate our basic approach.

5.1 Sampling in the Transform Space

We enclose the support of f in a sphere of radius R_1, i.e.,

$$S = \{(x, y, z) \in \mathbb{R}^3 \mid x^2 + y^2 + z^2 \leq R_1^2\}, \tag{5.1}$$

and the center of S lies at the origin.

In our experiment, the X-ray source is moving along a 3D curve parameterized by $\mathbf{\Phi}(\lambda)$ ($\lambda \in \Lambda$). We will restrict $\mathbf{\Phi}(\lambda)$ on a cylindrical surface with radius $R_2 \geq R_1$ (see Fig. 5-1). The axis of the cylinder is aligned with the z-axis. The principal direction of the projections is represented by the normalized vector $\boldsymbol{\gamma}(\lambda) = \mathbf{\Phi}(\lambda)/|\mathbf{\Phi}(\lambda)|$.

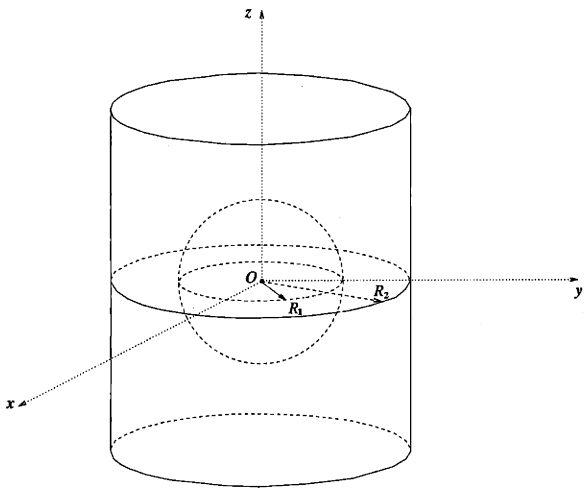

Figure 5-1: *Source orbit is confined on the outer cylinder*

5.1.1 Parallel-beam Case

In the parallel-beam case, the X-ray source is far away from the object ($R_2 \gg R_1$). The image plane perpendicular to the principal direction $\boldsymbol{\gamma}$ measures the density integrals along rays parallel to $\boldsymbol{\gamma}$. For the purpose of visualization, each image plane is represented by a plane with the same orientation but passing through the origin, it is called the **projection plane**. Denote by $L_{\boldsymbol{\gamma}}$ the projection plane perpendicular to $\boldsymbol{\gamma}$. We also call $\boldsymbol{\gamma}$ the **orientation** of $L_{\boldsymbol{\gamma}}$.

The *Fourier projection-slice theorem* is an efficient tool for approaching parallel-beam reconstruction. According to the projection-slice theorem, 2D Fourier transform of the measurements on each area detector provides spectral information on a plane in the 3D Fourier space. This plane in the Fourier domain is called the **spectral plane**. It passes through the origin and has the same orientation as the image plane. Denote the spectral plane perpendicular to γ by $\hat{L}_\gamma$. It is clear that L_γ and $\hat{L}_\gamma$ are oriented in the same direction.

Denote by $\mathcal{L}$ the orthogonal coordinate transform that rotates the tilted plane to the xy-plane. $\mathcal{L}$ has the following properties:

$$\mathcal{L}^{-1} = \mathcal{L}^T \quad \text{and} \quad \left| \frac{\partial(x, y, z)}{\partial(x', y', z')} \right| = +1. \tag{5.2}$$

The *projection-slice theorem* can be nicely illustrated by the following diagram:

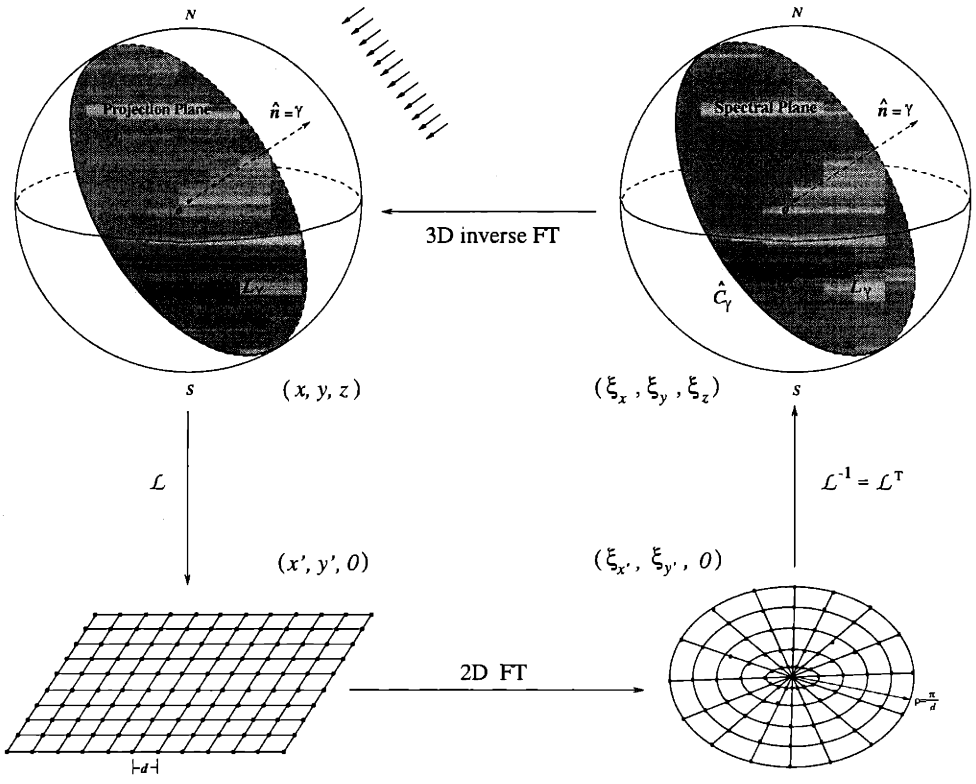

Figure 5-2: *Illustration of the parallel-beam reconstruction based on the Fourier projection-slice theorem.*

The data available from the parallel projections would cover the entire Fourier transform

space if and only if the family of projection planes passed by every point on the object sphere S (note in our definition all the projection planes pass through the origin). The inverse Fourier transform then can recover f. This is for the continuous case.

In practice, one can take only discrete measurements. According to Nyquist's sampling theorem, if the detectors are spaced at a distance d apart, then the frequency spectrum of the sampled image must be band-limited to (π/d) in order to avoid aliasing effects. Therefore on each spectral plane, there is a limit to the area where the transform is non-zero. Within that area (which we can take to be a circular disk for convenience) we assume the sampling to be uniform. Spectral content in between the samples on a spectral plane may be estimated by interpolation.

Another discretization takes place along the X-ray source orbit: only a finite number of projections are conducted. Spectral information that is not on any of the planes corresponding to the available projections needs to be interpolated from the available spectral data. Different from the interpolation on the 2D spectral planes obtained from each projection, the spectral interpolation at this stage is performed on the surface of a set of concentric spheres. Since the sampling conditions on these concentric spheres are different only by a scaling factor, it is sufficient to study only the sampling performance on the outer surface of the spectral sphere that is influenced by the source orbit. The ideal scenario for accurate interpolation and thereby stable reconstruction is that the resulting sampling density distribution on the surface of the spectral sphere is uniform. It turns out to be far from trivial to find a source orbit that approximates this ideal condition.

For simplicity, we consider the radius of the spectral sphere to be unit. Denote by $\hat{S}$ the spectral sphere. Denote by $\hat{C}_\gamma$ the great circle where $\hat{L}_\gamma$ meets with $\hat{S}$.

Assume that we start with a particular projection orientation, say γ^*. The continuous movement of the X-ray source on a nice and smooth orbit sets $\hat{C}_{\gamma^*}$ into a rigid rotation. Such rotation can be conveniently described in the following matrix form:

$$\boldsymbol{R}(\lambda) = \big(\boldsymbol{\gamma}'(\lambda),\ \boldsymbol{\gamma}(\lambda),\ \boldsymbol{\gamma}'(\lambda) \times \boldsymbol{\gamma}(\lambda)\big). \tag{5.3}$$

It is the orthogonal moving frame that we have encountered in Section 4.1.2.

It is clear now that the sampling condition in the 3D Fourier space corresponds to the sampling distribution on the spectral sphere swept by the family of great circles $\hat{C}_\gamma$ as the source orbit parameter, λ, varies over the indexing set Λ.

5.1.2 Cone-beam Case

Return to the cone-beam projection case, we find that this time we are dealing with a even more complicated problem, although the feature of rigid motion remains to be the underlying mechanism of the transform space covering. In this case it is in the Radon space. In the case of the parallel projection, all the spectral spheres are concentered at the origin. They duplicate the sampling pattern from each other and are equivalently characterized. However, in the Radon space, the Radon spheres are attached to every point in the object space. From the discussion in Section 4.1.2 we know that each cone-beam projection confines the backprojection orientations on a great circle on each of these Radon spheres, and the great circle is perpendicular to the source-to-point line. When the source moves, the great circle undergoes rigid rotation. However, the rotational pattern of the great circle on each Radon sphere depends on its location (see Fig. 5-3). As a result, the sampling condition of the Radon sphere varies from place to place.

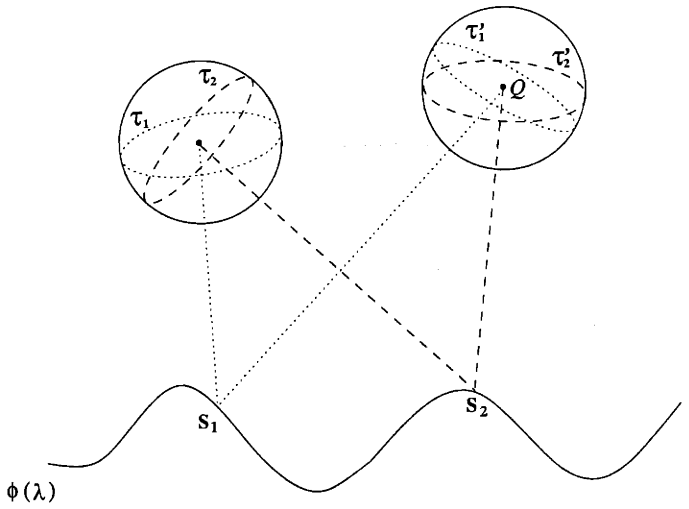

Figure 5-3: *Varying sampling patterns on the Radon spheres.*

Ideally, we would like every Radon sphere to be evenly sampled. Since the sampling pat-

tern of every Radon sphere differs from each other, designing a "good" source orbit which produces a considerably evenly-sampled Radon sphere everywhere in the object space is a challenging task. We can tell that the shape of the region under inspection is an important factor in selecting proper source orbits. The treatment of round and elongated objects should be different. Intuition might very well provide us some preferred candidates.

It turns out that in both parallel-beam and cone-beam cases, if we restrict ourselves to study only the roles played by the source orbit on the sampling performance, we need to solve the same basic problem, that is, how to characterize the sampling density distribution on a spherical surface swept by a set of great circles resulting from a rigid rotation.

5.2 A Preliminary Discussion on the Source Orbit

We stress here that the curve $\gamma = \Phi/|\Phi|$ is the projection of the source orbit onto the unit sphere through the origin. Some sample γ curves are illustrated in Fig. 5-4.

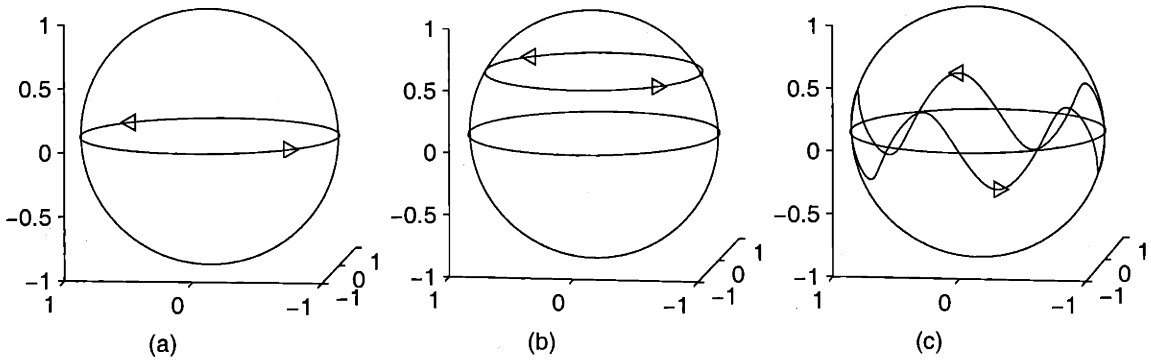

Figure 5-4: *Some sample source orbits projected ($\gamma = \Phi/|\Phi|$) on the unit sphere.*

Fig. 5-4 (a) and (b) represent two planar circular orbits at different altitudes — in (a) we have the orbit in the xy-plane, while it is elevated above that plane in (b). Orbit (c) illustrates a 3D sinusoidal path on the unit sphere. These are among the easiest orbits to implement considering mechanical limitations of the gantry motion, such as limited accelerations on the X-ray tube assembly (the sinusoidal orbit, e.g. requires an accelerating force that is simply proportional to the distance from the "neutral plane").

One way to explain the advantages of a sinusoidal orbit is to compare it to a circular orbit. It happens in (a) that the set of great circles all meet at the North and South poles as shown in Fig. 5-5(a), producing unequal sampling with very high density at the two poles and relatively poor sampling near the equator. To be exact, the sampling density varies proportionally to $\sec\eta$, where η is the latitude on the sphere. It is lowest near the equator, grows with latitude, and has singularities at the poles.

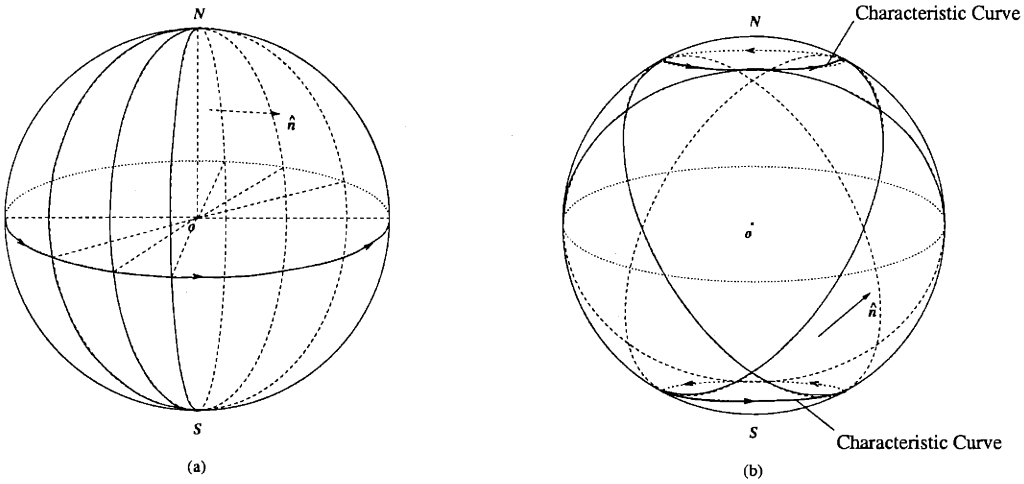

Figure 5-5: *Rotation of the great circles.*

Now we turn to case (b) where the projections are tilted. If α is the elevation of the planar (circular) orbit above the horizontal plane, then it can be shown that the sampling density varies as

$$\begin{cases} \dfrac{1}{\sqrt{\cos^2\alpha - \sin^2\eta}}, & \text{for } |\eta| < (\pi/2 - \alpha) \\ 0, & \text{for } |\eta| > (\pi/2 - \alpha) \end{cases} \tag{5.4}$$

where η is the latitude. This reduces to $\sec\eta$, the density for case (a), when $\alpha = 0$. Here the density at low altitude is increased from 1 to $\sec\alpha$ and the point singularity at the two poles is distributed over two small circles at latitude $\eta = \pm(\pi/2 - \alpha)$ (see Fig. 5-5(b)).

The improved uniformity in density is, however, achieved at the cost of transform information within two *shielded cones* (Fig. 5-6) around the z-axis, which is not available at all.

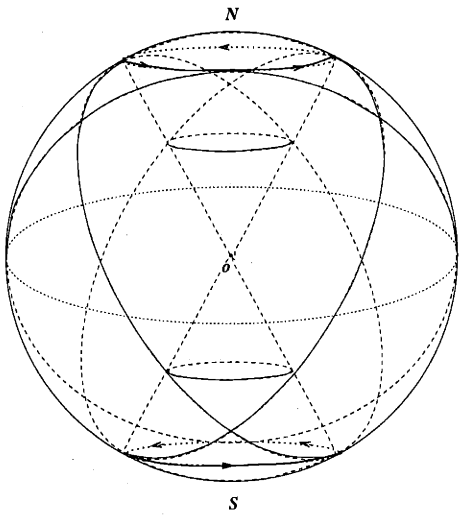

(b)

Figure 5-6: *The shielded cones.*

In order to cover the area on the sphere missing when using orbit (b), we can move the X-ray source in an up-and-down fashion as indicated in (c). The great circles meet the poles only when the source is positioned on the equator (which happens only a finite number of times).

This will provide an improvement in the uniformity of sampling at different parts of the sphere compared to that provided by a circular orbit. The sampling density near the poles and the equator can be effectively tuned by two parameters: the height of the sinusoidal curve and the number of times it crosses the central plane. This makes it possible to obtain a more uniform distribution. While it is likely that the "optimal" orbit is not in this particular family of curves, it should be noted that a similar discussion can be carried out for extended family of 3D curves.

5.3 Characteristic Curve

Let the **characteristic curve** ς be defined as the envelope of the family of great circles C_γ on the unit sphere centered at the origin. C_γ's are from the family

$$\left\{ C_\gamma \subset \mathbf{S}^2 \middle| C_\gamma \perp \boldsymbol{\gamma},\ \boldsymbol{\gamma} = \frac{\boldsymbol{\Phi}}{|\boldsymbol{\Phi}|} \right\}. \tag{5.5}$$

The characteristic curves of the planar (circular) orbits are rather simple: they are two poles for orbit (a) and two (small) circles for orbit (b) (Fig. 5-5). In fact, the missing contents are inside the convex hull formed by the family of 2D planes passing through the great circles. This convex hull can be described by the characteristic curve and its tangent field. An example will be given in Section 5.4.2. Now we focus on finding the equation for the characteristic curve.

Theorem 5.1 *The characteristic curve is generated by*

$$\varsigma = \pm \frac{\gamma \times \gamma'}{|\gamma \times \gamma'|}. \tag{5.6}$$

Proof: It is sufficient to verify that $\varsigma'(\lambda)$, the tangent of $\varsigma(\lambda)$, agrees with the tangent of the great circles at their intersections. $\varsigma'(\lambda)$ can be evaluated as follows

$$\begin{aligned}
\varsigma'(\lambda) &= \left(\frac{\gamma \times \gamma'}{|\gamma \times \gamma'|} \right)' \\
&= \frac{(\gamma \times \gamma')'}{|\gamma \times \gamma'|} + \frac{|\gamma \times \gamma'|'}{|\gamma \times \gamma'|^2} (\gamma \times \gamma') \\
&= \frac{\gamma \times \gamma''}{|\gamma \times \gamma'|} + \frac{(\gamma \times \gamma') \cdot (\gamma \times \gamma')'}{|\gamma \times \gamma'|^3} (\gamma \times \gamma') \\
&= \frac{\gamma \times \gamma''}{|\gamma'|} + \frac{(\gamma \times \gamma') \cdot (\gamma \times \gamma'')}{|\gamma'|^3} (\gamma \times \gamma') \\
&= \frac{\gamma \times \gamma''}{|\gamma'|} + \frac{|\gamma|^2 (\gamma' \cdot \gamma'') - (\gamma \cdot \gamma')(\gamma \cdot \gamma'')}{|\gamma'|^3} (\gamma \times \gamma') \qquad (5.7) \\
&= \frac{\gamma \times \gamma''}{|\gamma'|}. \qquad (5.8)
\end{aligned}$$

The last identity holds because $\gamma \cdot \gamma' = \gamma' \cdot \gamma'' = 0$, so the second term in Eqn. (5.7) is zero. Now, for a fixed orientation γ, C_γ is perpendicular to γ, together with $\gamma \times \gamma'' \perp \gamma$ we get

$$\frac{\gamma \times \gamma'}{|\gamma \times \gamma'|} \in C_\gamma. \tag{5.9}$$

Therefore, the great circle C_γ meets ς at $\dfrac{\gamma \times \gamma'}{|\gamma \times \gamma'|}$. From the last relation, the tangent of C_γ at the intersection with ς is perpendicular to both γ and $\gamma \times \gamma'$, therefore, parallel to $\gamma \times (\gamma \times \gamma')$. Moreover, we have for ς'

$$\left.\begin{array}{lll} \varsigma' \parallel \gamma \times \gamma'' & \Longrightarrow & \varsigma' \perp \gamma \\ \varsigma' \perp \varsigma,\ \varsigma \parallel \gamma \times \gamma' & \Longrightarrow & \varsigma' \perp \gamma \times \gamma' \end{array}\right\} \Longrightarrow \varsigma' \parallel \gamma \times (\gamma \times \gamma'). \quad (5.10)$$

It follows that the tangent of the great circle C_γ and the tangent of ς are both parallel to $\gamma \times (\gamma \times \gamma')$ at their intersection. From the above, we conclude that the family of the great circles and ς are cotangent. Eqn. (5.6) describes the envelope of C_γ's. ∎

5.4 A Case Study: Sinusoidal Source Orbit

5.4.1 Equation for a Sinusoidal Orbit

Assume that Φ is a sinusoidal curve on the cylinder. The curve can be parameterized by the *longitude* λ . Let the z-component of $\Phi(\lambda)$ be $\phi_3(\lambda) = hR_2 \sin(n\lambda)$, with hR_2 the *magnitude* (the maximum height) of $\Phi(\lambda)$, and n the *number of cycles* around the equator. We can use the parameterization $\Phi(\lambda) = R_2(\cos\lambda, \sin\lambda, h\sin n\lambda)$ and then project this cylindrical orbit onto the unit sphere using $\gamma(\lambda) = \Phi(\lambda)/|\Phi(\lambda)|$ (see Fig. 5-7).

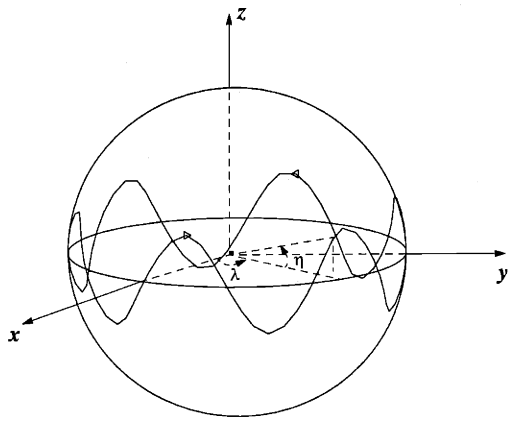

Figure 5-7: *A sinusoidal orbit projected onto the unit sphere.*

The 3D curve $\gamma(\lambda)$ crosses the equator $2n$ times when the source completes a whole orbit around the sphere. The curve $\gamma(\lambda)$ intersects the equator at $\lambda = m\pi/n$, $m = 0, 1, \cdots, 2n-1$. At these crossings,

$$\gamma(\frac{m\pi}{n}) = (\cos\frac{m\pi}{n}, \sin\frac{m\pi}{n}, 0), \tag{5.11}$$

$$\gamma'(\frac{m\pi}{n}) = (-\sin\frac{m\pi}{n}, \cos\frac{m\pi}{n}, \pm hn), \tag{5.12}$$

$$\gamma''(\frac{m\pi}{n}) = (-\cos\frac{m\pi}{n}, -\sin\frac{m\pi}{n}, 0). \tag{5.13}$$

where the sign of the $\pm hn$ term is that of $\cos(m\pi/n)$.

5.4.2 Characteristic Curve of the Sinusoidal Orbit

Fig. 5-8 and 5-9 plots ς near the South pole for sinusoidal orbits with different magnitudes h. As the magnitude of the orbits increases, the characteristic curve dilates to cover a larger area.

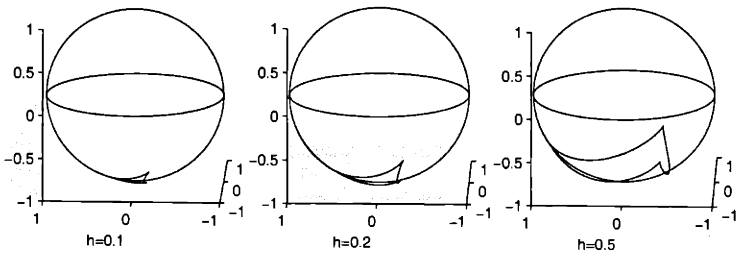

Figure 5-8: *Side view of the characteristic curve ς with varying magnitude h.*

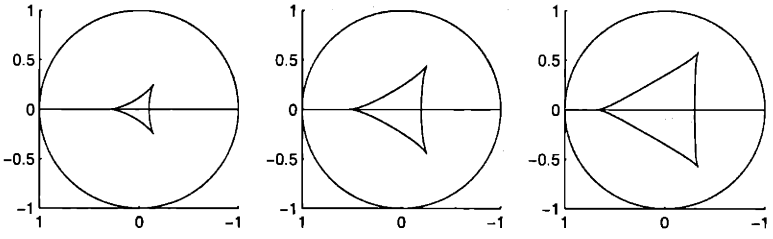

Figure 5-9: *Top view of the characteristic curve ς with varying magnitude h.*

It has been shown that a cusp appears each time when γ crosses the equator and orientation of the illumination is flipped. Since γ is a differentiable curve, from Eqn. (5.6) we know

that ς is differentiable as well. A cusp can only appear when the tangent vector is zero. This can be easily verified:

Lemma 5.1 *The characteristic curve of the sinusoidal orbit* $\Phi(\lambda) = R_2(\cos\lambda, \sin\lambda, h\sin n\lambda)$ *has zero tangent at* $\lambda = (m\pi)/n$ $(m = 0, 1, \cdots, 2n-1)$.

Proof: From Eqn. (5.11) and (5.13), $\boldsymbol{\gamma} \times \boldsymbol{\gamma}'' = 0$ at $\lambda = (m\pi)/n$ $(m = 0, 1, \cdots, 2n-1)$. It quickly follows from Eqn. (5.8) that $\boldsymbol{\varsigma}' = 0$. Hence, the characteristic curve has zero velocity at the crossings. ∎

Fig. 5-10 and 5-11 demonstrate the roles played by the number of cycles n. Each time $\gamma(\lambda)$ crosses the equator, the orientation of the projections is flipped (or mathematically speaking, the tangent vector $\boldsymbol{\varsigma}'(\lambda)$ descends to zero and then suddenly changes its direction) so that we see a cusp on the characteristic curve.

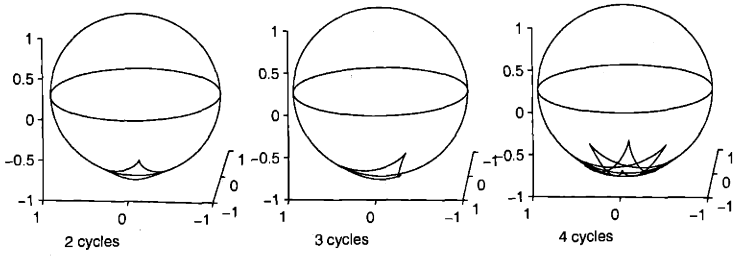

Figure 5-10: *Side view of the characteristic curve* $\boldsymbol{\varsigma}$ *with different* n.

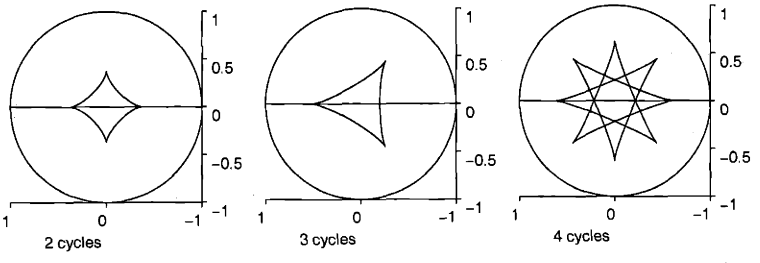

Figure 5-11: *Top view of the characteristic curve* $\boldsymbol{\varsigma}$ *with different* n.

The characteristic curve has $2n$ cusps for even n, agreeing with the number of times the X-ray source passes the equator. As for odd n, $\boldsymbol{\gamma}$ is symmetric with respect to the origin (i.e. if $\boldsymbol{\gamma}$ is on the orbit, then so is $-\boldsymbol{\gamma}$) which means that the characteristic curve will retrace

itself a second time so it generates only n distinct cusps (i.e. half the number of crossings). At the crossings, the projection planes happen to be vertical and passing through the poles.

To acquire more intuitive understanding of the limiting process as the source approaches its zero crossings, we can project the characteristic curve onto a horizontal plane $\boldsymbol{H}$ as shown in Fig. 5-12.

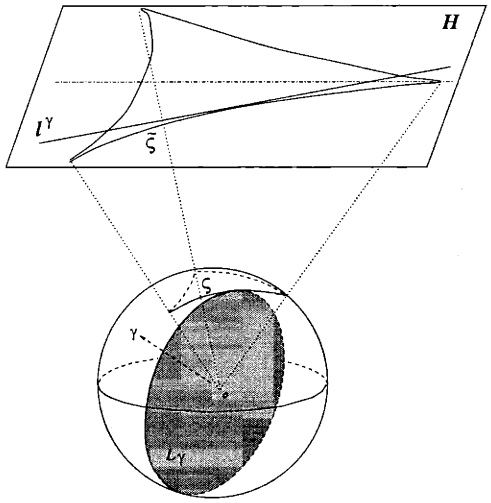

Figure 5-12: *Project ς onto a horizontal plane $\boldsymbol{H}$ through the origin.*

Denote by $\tilde{\varsigma}$ the projection of ς from the origin onto $\boldsymbol{H}$. It is easy to verify that the projections of the great circles (as well as the 2D planes passing by them) are straight lines tangent to $\tilde{\varsigma}$.

Lemma 5.2 *While λ approaching $(m\pi)/n$ $(m = 0, 1, \cdots, 2n-1)$ from left to the right, the limiting angle between the unit tangents of the curve $\tilde{\varsigma}$ is π.*

Proof: By periodicity and symmetry, we only need to prove for $\lambda \to 0^{\pm}$. As λ gradually approaches 0 from 0^- and 0^+, it can be checked that the sign of each component in $\tilde{\boldsymbol{\varsigma}}'$ is switched from $\tilde{\boldsymbol{\varsigma}}'(-\lambda) = (\tilde{\varsigma}_1', \tilde{\varsigma}_2', 0)$ to $\tilde{\boldsymbol{\varsigma}}'(\lambda) = (\tilde{\varsigma}_1', -\tilde{\varsigma}_2', 0)$ (via straightforward calculation of $\boldsymbol{\gamma} \times \boldsymbol{\gamma}''$). And the asymptotic behavior of $\tilde{\boldsymbol{\varsigma}}'$ is: $\tilde{\varsigma}_1' \sim o(\lambda^2)$ and $\tilde{\varsigma}_2' \sim o(\lambda)$ as $\lambda \to 0$. We conclude that the unit tangent goes to the opposite direction after the zero-crossing. ∎

Lemma 5.3 and Lemma 5.4 lead us to the following:

Lemma 5.3 *The convex hull enclosed by the family of the 2D planes passing by the family of great circles C_γ is empty for $n \geq 1$.*

Proof: For $n \geq 1$, there are more than two cusps as the results of the zero crossings. To see that the convex hull is empty, we only need to walk counterclockwise along the curve $\tilde{\varsigma}$ and keep looking at our left (see Fig. 5-13).

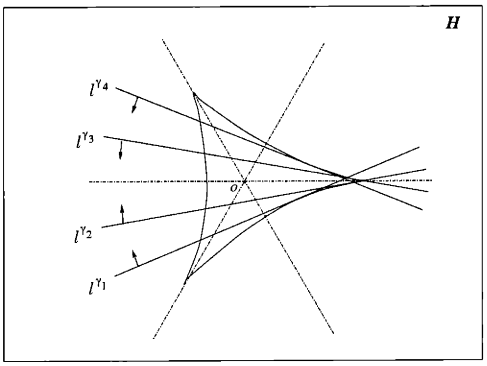

Figure 5-13: *Projection of the 2D planes passing by the great circles are tangent to $\tilde{\varsigma}$. The union of their left half space fill the entire space.*

As we progress, the unit normal changes continuously till we pass through a cusp and the normal direction suddenly flips to its opposite. Hence the half space on our left will sweep through the entire space when we complete traveling on the closed curve $\tilde{\varsigma}$. It yields an empty convex hull. ∎

5.4.3 Sampling Performance of the Sinusoidal Orbit

An important feature of the characteristic curve is its tangent vector. $|\varsigma'(\lambda)|$ tells us how fast the great circle is moving on the envelop as the X-ray source moves in its orbit. From this basic fact we can conclude that the sampling density at the cusps are infinite because the velocity $|\varsigma'|$ at those points is zero (see Lemma 5.1).

With the sinusoidal source curve, sampling density near the cusps can be effectively reduced without impacting the sampling performance in other areas of the sphere be varying the discrete sampling steps on the source curve, i.e., sampling more sparsely near the zero crossings of the sinusoidal orbit and more densely near the flat portions of the curve. In

addition, we observe that as h increases, the sampling frequency near the equator improves. For fixed h, the number of times $(2n)$ that the sinusoidal curve crosses the equator affects the sampling density near the two poles (see Fig. 5-14).

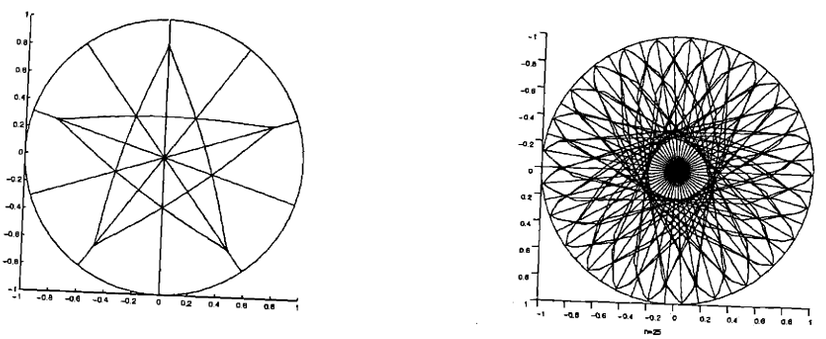

Figure 5-14: *Characteristic curves:* $n = 5$ *(left) and* $n = 25$ *(right).*

Any missing transform content would be in the convex hull surrounded by the family of 2D planes passing through the origin. In the case of sinusoidal source orbit, this convex hull is empty as long as $n \geq 1$.

Interestingly, the sampling performance of a sinusoidal orbit with $n = 1$ (Fig. 5-15) is similar to that of a tilted circular orbit which has singularity at the two poles. In this case, the characteristic curve shrinks to a tiny area away from the z-axis with three distinctive cusps. The result is that the sphere is completely covered with high density near the characteristic curve. Note that the picture in Fig. 5-15 (left) is zoomed in.

A sinusoidal orbit with $n = 1/2$ performs somewhat like a circular orbit above the equator. There is a nonempty convex hull surrounded by the family of great circles which means some transform information is not accessible.

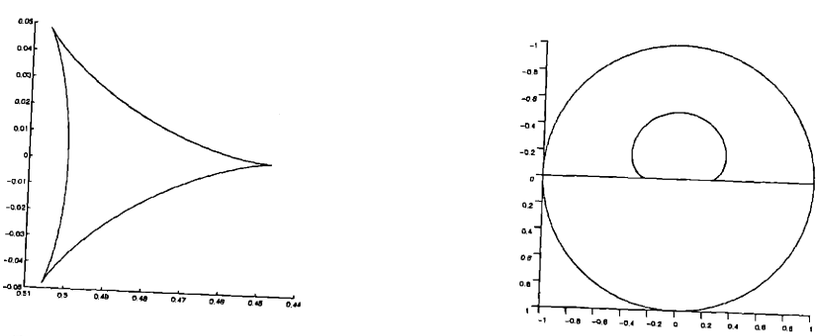

Figure 5-15: *Characteristic curves:* $n = 1$ *(left, zoomed) and* $n = 1/2$ *(right).*

5.5 Summary and Future Ahead

To conclude this thesis, we overview our short journey. We have expanded three earlier theoretical results on cone-beam reconstruction. The significant role played by geometry during the inverse is revealed. It is clear now that the scanning geometry determines the dual space decomposition as well as the structure of the reconstruction algorithm. A novel interpretation of the Radon inverse is presented through our reformulation which has the capability of handling various scanning geometries. Within this framework, a family of exact, FBP-typed algorithms are arrived following the lead by Tuy, Smith and Grangeat. Their efficiency and stability vary by the nature of the algebraic transform used to carry the cone-beam data into the Radon transform domain.

New challenges come along. Particularly, the optimal sampling schemes and related weighting techniques shall be the focus of future research. Our study shows that sampling in the Radon space is fundamentally different from what we have been dealing with in the Euclidean space. Complexity arises in the underlying sampling mechanism. A few mathematical devices developed in this thesis can be used to study the sampling performance of various source orbits. They shall be combined with a specified application and system, as well as empirical study to produce more fruitful results.

Related and interesting theoretical work on 3D reconstruction by Gelfand [Gelfand, 1986] and Orlov [Orlov, 1975] are not included in our discussion. Further studies are expected to draw comparison and possible connection. Another remission lies in the area of the helical cone-beam CT [Kudo, 1991, Weng, 1993], where the X-ray source is traversing on a helical source orbit and the detector size is considerably smaller than the scanned object. In such a system, data is truncated along the longitudinal direction. A mosaic paving is needed in order to obtain the Radon transform derivative on those planes passing by the object [Danielsson, 1997]. It brings a even more challenging problem on sampling optimization. However, the basic reconstruction algorithm remains unchanged.

Blessed by Radon, tomographic research constantly grow while in turn enrich the theory; Re-animated by human imagination, CT industry continues to try its wings and fly into its destiny: to make this world a healthier, kinder, and more joyful place to live.

Bibliography

[Axelsson, 1994] C. Axelsson and P.E. Danielsson "Three-dimensional reconstruction from cone-beam data in $O(N^3 \log N)$ time." *Phys. Med. Biol., 39*, 1994, pp. 477-491

[Carmo, 1976] M. P. do Carmo "Differential Geometry of Curves and Surfaces." *Prentice-Hall Inc.*, 1976

[Danielsson, 1997] P.E. Danielsson, P. Edholm, J. Eriksson and M. Magnusson-Seger "Towards Exact 3D-reconstruction for Helical Cone-beam Scanning of Long Objects" *Int. Meet. on Fully Three-Dim. Im. Rec. in Rad. and Nuc. Med.*, Nemacolin, PA, USA, June 25-28, 1997, pp. 141-144

[Defrise, 1994] M. Defrise and R. Clack "A cone-beam reconstruction algorithm using shift variant filtering and cone-beam backprojection. " *IEEE Trans. Med. Imag., Vol. 13*, 1994, pp. 186-195

[Feldkamp, 1984] L.A. Feldkamp, L.C. David and J.W. Kress "Practical cone-beam algorithm." *J. Opt. Soc. Am. A., Vol. 1, No. 6*, 1984, pp. 612-619

[Finch, 1985] D. Finch "Cone beam reconstruction with sources on a curve." *SIAM J. Appl. Math, Vol. 45*, 1985, pp. 665-673

[Gelfand, 1986] I. M. Gelfand and A. B. Goncharov "Reconstruction of finite functions from integrals over straight lines through given points in space." *Dokl. 290*, 1986, pp. 1037-1040

[Grangeat, 1991] P. Grangeat "Mathematical framework of cone beam 3d reconstruction via the first derivative of the Radon transform." *Mathematical methods in tomography, Lecture notes in mathematics 1497*, 1991. pp. 66-97

[Helgason, 1999] S. Helgason "The Radon Transform." *2nd Edition, Birkhäuser*, 1999

[Hilbert, 1952] D. Hilbert and S. Cohn-Vossen "Geometry and the Imagination." *Chelsea Publishing Company*, 1952

[Horn, 1978] B. K. P. Horn "Density Reconstruction Using Arbitrary Ray Sampling Schemes." *Proceedings of the IEEE*, Vol. 66, No. 5, May 1978, pp. 551–562.

[Horn, 1979] B. K. P. Horn "Fan-Beam Reconstruction Methods." *Proceedings of the IEEE*, Vol. 67, No. 12, December 1979, pp. 1616–1623.

[Kirillov, 1961] A. A. Kirillov "On a problem of I.M. Gel'fand." *Sov. Math. Dokl. 2*, 1961, pp. 268-269

[Kobayashi, 1963] S. Kobayashi and K. Nomizu "Foundation of differential Geometry." *John Wiley & Sons Inc.*, 1963

[Kudo, 1991] H. Kudo and T. Saito "Derivation and implementation of a cone-beam reconstruction algorithm for nonplanar orbits." *IEEE Trans. Med. Imag., Vol. 13*, 1994, pp. 196-211

[Kudo, 1994] H. Kudo and T. Saito "Helical-scan Computed Tomography Using Cone-Beam Projections" *Conference Record IEEE Nuc. Sci. Symp. and Med. Imag. Conf*, 1991

[Marr, 1981] R. B. Marr, C. Chen, P. C. Lauterbur "On two approaches to 3D reconstruction in NMR zeugmatography." *Mathematical Aspects of Computerized Tomography* edited by G. T. Herman and F. Natterer, Springer-Verlag, Berlin, 1981

[Mundy, 1992] "Geometric Invariance in Computer Vision." *Edited by Mundy and Zisserman, MIT Press*, 1992

[Natterer, 1986] F. Natterer "The Mathematics of Computerized Tomography." *John Wiley & Sons Ltd and B. G. Teubner, Stuttgart*, 1986

[Orlov, 1975] S. S. Orlov "Theory of three-dimensional reconstruction. II: The recovery operator" *Kristallographiya 20*, 1975, pp. 701-709

[Poularikas, 2000] "The transforms and applications handbook." *Edited by Alexander D. Poularikas, 2nd Ed., CRC Press & IEEE Press*, 2000

[Radon, 1917] J. Radon "Über die Bestimmung von Funktionen durch ihre Integralwerte längs gewisser Mannigfaltigkeiten" *Ber. Verh. Sächs. Akad. Wiss. Leipzig. Math. Nat. Kl.*, Vol. 69, pp. 262–277, 1917.

[Smith, 1985] B. D. Smith "Image reconstruction from cone-beam projections: necessary and sufficient conditions and reconstruction methods." *IEEE Trans. Med. Imag., Vol. 4*, 1985, pp. 14-25

[Tuy, 1983] H. K. Tuy "An inversion formula for cone-beam reconstruction." *SIAM J. Appl. Math, Vol. 43*, 1983, pp. 546-552

[Wang, 1999] X. Wang and R. Ning "A cone-beam reconstruction algorithm for circle-plus-arc data acquisition geometry." *IEEE Trans. Med. Imag., Vol. 18, No. 9*, 1999, pp. 815-824

[Weng, 1993] Y. Weng, G.L. Zeng and G.T. Gullberg "A reconstruction algorithm for helical cone-beam SPECT." *IEEE Trans. Nuc. Sci., NS-40*, 1993, pp. 1092-1101